

ÉCOLE POLYTECHNIQUE FÉDÉRALE DE LAUSANNE
MECHANICAL ENGINEERING FACULTY
ME-474
NUMERICAL FLOW SIMULATION

Flow Analysis in a Rotor-Stator Stage of an Axial Compressor

Investigating a Case Study of Turbomachinery Design

Lecturer: Edouard Boujo

April 29, 2024

Group 3

Gabriele Furlan 341760 gabriele.furlan@epfl.ch
Christoph Pabsch 342300 christoph.pabsch@epfl.ch
Lorenz Veithen 346364 lorenz.veithen@epfl.ch



Contents

List of Figures	iii
List of Tables	iv
Nomenclature	v
1 Introduction	1
2 Literature Review	2
3 Problem Formulation	4
3.1 Geometry	4
3.1.1 Presentation of the Geometry	4
3.1.2 Characteristic Dimensions	5
3.1.3 Symmetry and Periodicity of the Problem	5
3.2 Physical Modelling and Hypotheses	6
3.2.1 Modelling Strategy	6
3.2.2 Physical Modelling	7
3.2.3 Fluid Properties	8
3.2.4 Turbulent Flow Calculation	8
3.3 Boundary Conditions, External Forces and Initial Conditions	8
3.3.1 Boundary Conditions	9
3.3.2 Initial Conditions	10
4 Simulation Details	11
4.1 Meshing	11
4.1.1 Mesh Type	11
4.1.2 Cell Type	12
4.1.3 Size and Number of Cells	12
4.1.4 Final Mesh	13
4.2 Numerical Methods	15
4.2.1 Spatial Discretization Method	15
4.2.2 Type of Simulation and Solver	15
4.2.3 Solution Options	16
4.3 Mesh Size Convergence Study	17
4.3.1 Presentation of the Different Meshes	17
4.3.2 Frozen Rotor Stator Simulation	18
4.3.3 Estimation of the Relative Error	21
4.3.4 Choice of the Mesh	22
4.3.5 Validation of Y+	22
5 Results and Discussion	23
5.1 Setup Summary	23
5.2 Solution Convergence	23
5.3 General Flow Characteristics	25

5.4 Flow Around the Airfoils	31
5.5 Comparison with Frozen Rotor-Stator Case	32
6 Conclusion	35
References	37

List of Figures

2.1	Contour of Mach number at chock point, design point and numerical stall conditions [5]	2
2.2	Velocity contour for locked rotor operation [6]	2
2.3	Mach number contour for free-torque operation [6]	2
2.4	Velocity vector field along rotor blade [8]	3
3.1	Three-dimensional rotor-stator stage [11]	4
3.2	Typical geometry of a rotor-stator stage [1]	4
3.3	Subsonic optimal airfoil geometries from compressors	5
3.4	Geometry sketch in SpaceClaim	6
3.5	Sketch of the different outer domain boundary conditions applied	9
4.1	Inflation mesh around the airfoils boundary layer	11
4.2	Extension inflation mesh at the airfoils wake	11
4.3	Sketch of all refinement applied on the mesh	13
4.4	Final mesh used in this study	13
4.5	Orthogonality metrics of the final mesh used in this study	14
4.6	Skewness metrics of the final mesh used in this study	14
4.7	Aspect ratio metrics of the final mesh used in this study	14
4.8	Coarsest mesh of the convergence study (global element size of 25.3125 mm)	18
4.9	Finest mesh of the convergence study (global element size of 2.2222 mm)	18
4.10	Static pressure on the coarsest mesh in the convergence study (global element size of 25.3125 mm)	19
4.11	Velocity magnitude on the coarsest mesh in the convergence study (global element size of 25.3125 mm)	19
4.12	Static pressure on the finest mesh in the convergence study (global element size of 2.2222 mm)	20
4.13	Velocity magnitude on the finest mesh in the convergence study (global element size of 2.2222 mm)	20
4.14	Evolution of the pressure difference from the coarsest to the finest mesh	20
4.15	Evolution of the velocity at outlet from the coarsest to the finest mesh	20
4.16	Incremental variation of the pressure difference from the coarsest to the finest mesh	21
4.17	Incremental variation of the velocity at outlet from the coarsest to the finest mesh	21
4.18	Variation of the relative error for the pressure difference	21
4.19	Variation of the relative error for the velocity at outlet	21
4.20	Difference with respect to finest mesh for the pressure difference	21
4.21	Difference with respect to finest mesh for the velocity at outlet	21
4.22	Y+ around the blades in the steady simulation	22
4.23	Y+ around the blades in the unsteady simulation	22
5.1	Inlet static pressure	24
5.2	Scaled residuals over time	24
5.3	Inlet mass flow rate	25
5.4	Outlet mass flow rate	25
5.5	Static pressure contours in the domain at $t = 0.166$ s	26

5.6	Velocity vector field colour per gauge static pressure at $t = 0.166\text{ s}$ (using a limited colour bar range)	26
5.7	Velocity magnitude contours on the domain at $t = 0.166\text{ s}$	27
5.8	Contours of the velocity components at $t = 0.166\text{ s}$	27
5.9	Streamlines of the fluid through the axial compressor at $t = 0.166\text{ s}$	28
5.10	Static temperature contour at $t = 0.166\text{ s}$	28
5.11	Density contour at $t = 0.166\text{ s}$	28
5.12	Density contour of the flow at $t = 0.166\text{ s}$ after excluding the minimum of the domain . .	29
5.13	Turbulent intensity of the flow at $t = 0.166\text{ s}$	29
5.14	Turbulent kinetic energy of the flow at $t = 0.166\text{ s}$	29
5.15	Velocity magnitude contour of different subsequent time instants	30
5.16	Streamlines around the airfoils coloured by static pressure at $t = 0.166\text{ s}$ (modified from ANSYS)	31
5.17	Recirculation of the flow behind the stator coloured by velocity magnitude at $t = 0.166\text{ s}$	31
5.18	Pressure coefficient curves on the rotor and stator at $t = 0.166\text{ s}$	32
5.19	Velocity contours in steady state	33
5.20	Velocity vector field in steady situation	33
5.21	Velocity vector field in unsteady situation	33
5.22	Pressure contour in steady situation	34
5.23	Pressure contour in unsteady situation	34

List of Tables

3.1	Geometry specifics	5
3.2	Fluid properties used in the simulation (default values in Fluent for air)	8
4.1	Refined regions and boundaries and their element or edge size.	13
4.2	Refined regions and boundaries with respect to the overall mesh element size	18
4.3	Properties of meshes used in the convergence study	18
5.1	Inlet flow characteristics used as free stream quantities	32

Nomenclature

BC - *Boundary Condition*

BSL - *Boundary Separation Layer*

CAD - *Computer Aided Design*

CFD - *Computational Fluid Dynamics*

DLR - *Deutsches Institut für Luft- und Raumfahrttechnik (German Aerospace Center)*

DM - *Design Modeler*

IC - *Initial Condition*

ODE - *Ordinary Differential Equations*

PDE - *Partial Differential Equations*

FVM - *Finite Volume Method*

RANS - *Reynolds Averaged Navier Stokes*

UD - *Upwind Differencing*

TKE - *Turbulent Kinetic Energy*

Latin Letters	Quantity	Symbol Unit
A	Surface	m^2
a	Speed of sound	$\frac{m}{s}$
CFL	Courant-Friedrichs-Lewis condition	$[-]$
C_p	Specific heat	$\frac{J}{kg \cdot K}$
e	Internal energy	J
\vec{F}	External body forces vector	N
\vec{g}	Gravitational acceleration vector	$\frac{m}{s^2}$
h	enthalpy	J
h_j	Species enthalpy	J
I	Unit tensor	—
\vec{J}_j	Diffusion flux of species vector	m^2/s
k	Thermal conductivity	$\frac{W}{m \cdot K}$
k	Refinement factor mesh	$[-]$
k_{eff}	Effective heat conductivity	$W/(mK)$
L	Characteristic length	m
M_{max}	Maximum Mach number across the system	$[-]$
M_W	Molecular weight	$\frac{kg}{mol}$
\vec{n}	Outward normal vector	$[-]$
p	Gauge pressure	Pa
p	Static pressure	Pa
p_{op}	Operating pressure	Pa
p_∞	Freestream pressure	Pa
R	Radial position	m
R	Universal gas constant	$\frac{kg \cdot m^2}{s^2 \cdot K \cdot mol}$
Re	Reynolds number	$[-]$
S	Source of mass	$\frac{W}{m^3}$
S_m	Source of mass	$\frac{kg}{s}$

t	Time variable	s
T	Temperature	K
u	Upward velocity rotor	$\frac{m}{s}$
u_{max}	Maximum flow velocity across the system	$\frac{m}{s}$
\vec{u}	Vector of unknowns	[$-$]
V	Volume	m^3
\vec{V}	Velocity vector	$\frac{m}{s}$
V_∞	Freestream fluid velocity	$\frac{m}{s}$
x m	Global mesh element size	mm
Y^+	Dimensionless wall distance	[$-$]

Greek Letters	Quantity	Symbol Unit
Γ	Fraction of thermal conductivity over specific heat capacity	$\frac{W \cdot kg}{J \cdot m}$
ω	Rotational velocity rotor	rad
ρ	Density	$\frac{kg}{m^3}$
ρ_∞	Freestream fluid density	$\frac{kg}{m^3}$
$\tau^=$	Stress tensor	Pa
μ	Dynamic viscosity	$\frac{kg}{m \cdot s}$
μ_M	Molecular viscosity	$\frac{kg}{m \cdot s}$
ν	Kinematic viscosity	$\frac{m^2}{s}$
Φ	Unknown variable	[$-$]
τ_{eff}	Effective stress tensor	Pa
κ	Turbulent kinetic energy	$\frac{m^2}{s^2}$
ϵ	Rate of dissipation of TKE per unit mass	$\frac{m^2}{s^3}$
ω	Turbulent frequency	$\frac{rad}{s}$
ν_t	Turbulent viscosity	$\frac{s}{m^2}$

Introduction 1

The present report has the goal of investigating stator-rotor 2D interaction in an axial compressor. Axial compressors consist in a series of stages, composed of rotor and stator, in order to achieve high pressure in a gradual way. The kinetic energy of the fluid (usually air) is increased by the rotor, while in the stator the static pressure increases at the expense of the fluid velocity [1]. In the field of turbomachinery, axial compressors are widely used in power generation or in the aeronautical field. The study is focused on the analysis of the evolution of velocity and pressure fields through a rotor-stator stage of a compressor. In particular, it is evaluated whether the compressor fulfills its compressing task by investigating the pressure difference over the rotor-stator stage.

The method used for the analysis of the compressor stage involves the use of different resources. The data needed to create the geometry, in particular the measures of the rotor and stator blade shapes, are taken from the German Aerospace Center [2]. The software SpaceClaim has been used to produce the 2D geometry. Due to the upward rotor movement, increasing the kinetic energy of the fluid, a sliding mesh is needed for the rotor region to simulate the compressor stage. The final mesh is obtained using a convergence study based on convergence of the pressure difference as well as the outlet velocity of the rotor-stator stage. A snapshot of the converged solution from ANSYS Fluent is finally used to analyse compression of the rotor-stator stage presented in this report. The overall goal of this work is to determine if the selected geometry is able to compress the flow and to investigate how the compression process takes place.

The report is structured as follows: First, a literature review is performed in chapter 2, summarizing results of comparable studies. The problem of the present study is consequently specified in chapter 3, by presenting the geometry, physical modelling as well as the boundary and initial conditions. The following chapter 4 explains how the simulation was set up and presents the mesh size convergence study leading to the final mesh used in this study. The results are then presented and discussed in chapter 5. A final conclusion is drawn in chapter 6, accompanied by recommendations for future studies.

Literature Review 2

Several studies regarding Computational Fluid Dynamics (CFD) in axial compressors have been carried out, showing the potential that this type of machines have in industry. Barberi et al. [3] have analyzed steady and unsteady CFD predictions for gas turbine engines in axial compressors in order to evaluate performances and compare them with experimental results to help the design phase. Ayesha Khan et al. [4] have investigated the use of CFD techniques on a transonic axial compressor in order to monitor the degradation of the compressor over time. The flow simulation was useful to analyze the interaction between tip leakage flow and the secondary flow and the effect on the compressor performance. Kumar et al. [5] have investigated the design and flow behaviour in an axial compressor for small gas turbine application using ANSYS CFX. In Fig. 2.1, the obtained contours of the Mach number are shown.

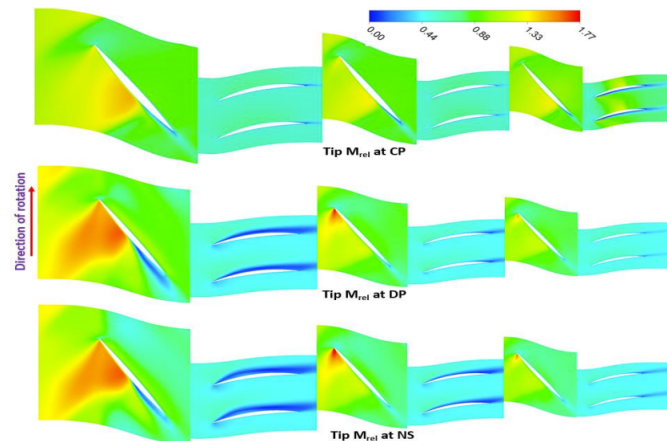


Figure 2.1: Contour of Mach number at chock point, design point and numerical stall conditions [5]

Furthermore, Ferrer-Vidal et al. [6] have used CFD validation applied to an axial compressor to evaluate performance in locked rotor and zero-torque windmilling characteristics. The resulting profiles at locked and free-torque rotor are displayed in Fig. 2.2 and 2.3, obtained using ANSYS CFX. Similar results are expected for the present report.

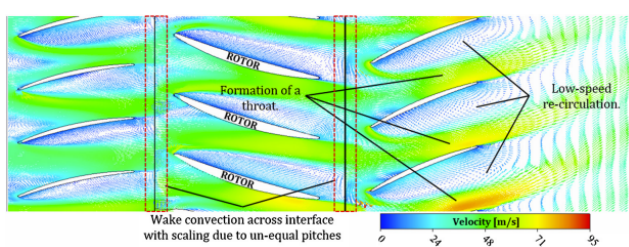


Figure 2.2: Velocity contour for locked rotor operation [6]

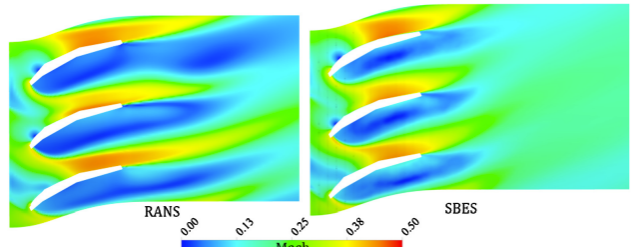


Figure 2.3: Mach number contour for free-torque operation [6]

CFD techniques have also been used by Baretter et al. [7] to observe the variation of azimuthal flow distortion at the axial compressor outlet, that can affect operation performance and stability. The case study simulates a pressure disturbance imposed using an inlet boundary condition in order to analyze the development of the swirl at the outlet. Moreover, Shobhavathy et al. [8] have used CFD, and ANSYS Fluent in particular, to investigate the flow evolution in a single stage transonic axial flow compressor. To validate the flow solver, steady simulations have been performed. The results achieved are validated with experimental data. In Fig. 2.4, the resulting velocity vector field is shown.

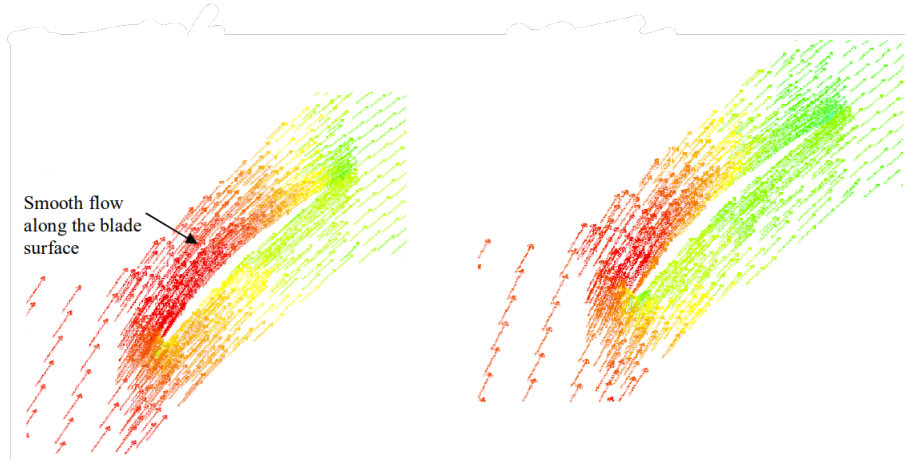


Figure 2.4: Velocity vector field along rotor blade [8]

Problem Formulation 3

In this chapter, the CFD formulation of the problem will be presented. First, the rotor-stator geometry will be presented in section 3.1, then section 3.2 will outline the main assumptions and models using to represent the physics of the flow. Finally, the Boundary Conditions (BCs) and Initial Conditions (IC) will be outlined in section 3.3.

3.1 Geometry

This section aims at detailing the geometry of the problem. First the general geometry will be presented, followed by the quantitative measures of the different items present.

3.1.1 Presentation of the Geometry

The problem being investigated considers a two-dimensional simplification of a rotor-stator stage. Such simplification was used in multiple studies [9, 10] to investigate the certain flow patterns and obtain first order accurate approximations of the flow properties with respect to the real three-dimensional system. Furthermore, such simplification permits to largely reduce the computational complexity of the problem, allowing to obtain significant results within the short timeframe of the project. Such typical geometry is shown in Figure 3.2.

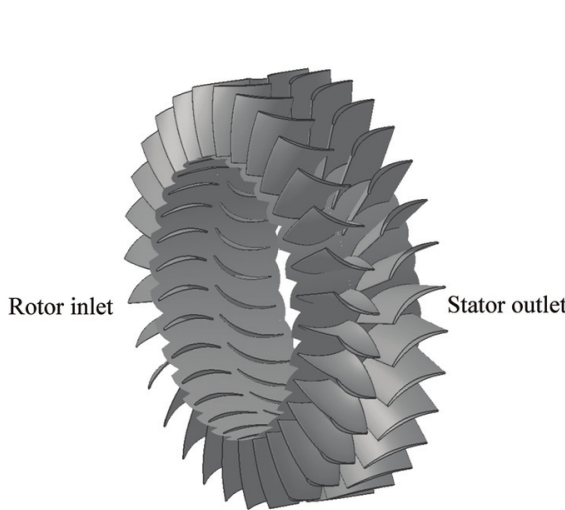


Figure 3.1: Three-dimensional rotor-stator stage [11]

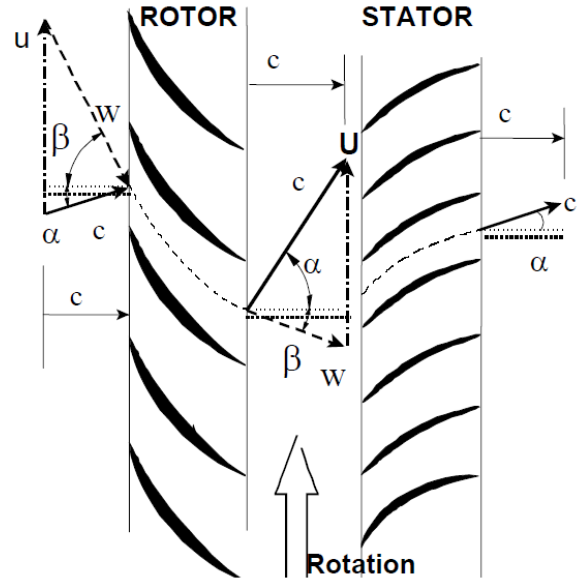


Figure 3.2: Typical geometry of a rotor-stator stage [1]

As can be seen in Figure 3.2, one stage of such system is composed of two rows of airfoils, called the rotor and stator respectively. In a real three-dimensional stage (see Figure 3.1), the rotor row

has a rotational velocity, which can be seen as an upward translation of the rotor row in the 2-D simplification, given by an upward velocity $u = \omega R$ where ω is the rotational velocity of the rotor row and R is the radial position that is being investigated. The stator row however is always fixed and serves to compress the flow while redirecting it towards the right direction.

3.1.2 Characteristic Dimensions

For this study, the geometry measures, required to create rotor and stator blades, were extracted from a database of optimal airfoils for axial compressor design from the German Aerospace Center (DLR) [2]. Those two airfoils are shown in Figure 3.3.



(a) Rotor airfoil geometry [2]



(b) Stator airfoil geometry [2]

Figure 3.3: Subsonic optimal airfoil geometries from compressors

These airfoils are stated to be optimal for the case of a subsonic axial compressor. Furthermore, the profile of the airfoil was obtained using the 3D-curve option in Design Modeller (DM) which uses B-splines to interpolate the different points. Two of them were used in each row for better visualisation purposes.

The data concerning the rest of the geometry is given in Table 3.1. Note that the unit system used in DM and SpaceClaim was in meters (SI units).

Table 3.1: Geometry specifics

Component	Dimensions
Rotor chord length	240 mm
Stator chord length	340 mm
Gap between rotor and stator	50 mm
Gap between blades	170 mm
Rotor tilt angle	-50°
Stator tilt angle	20°
Inlet and outlet depth	200 mm

The dimensions of the problem are further shown in Figure 3.4. Most of this data was taken from a Computer Aided Design (CAD) file [12], however, the vertical gap between the blades was taken to be the same for both the rotor and stator rows in order to simplify the geometry. The same assumption was made in other resources such as the ANSYS Fluent User Guide 2021 [13] in an example of the sliding mesh option.

Furthermore, the space before and after the stage was kept relatively small compared to the whole geometry, as there would be following and preceding stages in practice. Hence, the inlet and outlet were kept close to the stage itself to stay closer to the true physical system.

3.1.3 Symmetry and Periodicity of the Problem

The three-dimensional geometry, as shown in Figure 3.1, can be seen as axisymmetric periodic. Translating to the 2-D case considered, periodicity is imposed at the upper and lower part of the

domain in all regions (inlet, rotor, stator, outlet) as it can be argued that the flow is approximately the same at all azimuthal positions in the 3-D case.

Furthermore, the upward translation of the rotor row is periodic. This aims to model that one rotor airfoil is always followed by another one in the true 3-D geometry. This means that the inlet and stator regions are fixed in space while the rotor region slides up and repeats itself when the extreme upward position is reached. The complete geometry is shown in Figure 3.4.

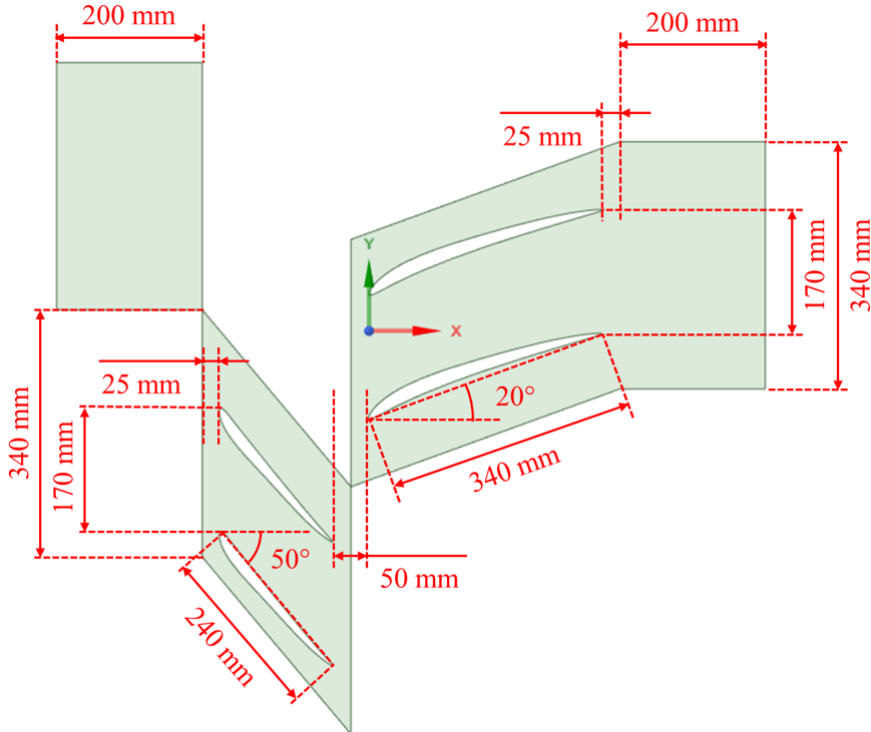


Figure 3.4: Geometry sketch in SpaceClaim

3.2 Physical Modelling and Hypotheses

In this section, the physical modelling of the problem analysed is presented. This includes the physical behaviour and models used, as well as the constant fluid properties. This section will follow the same path as is needed to enter the information in ANSYS Fluent in order to run such simulation.

3.2.1 Modelling Strategy

The main challenge in the modelling of the system is to represent a physical system that originally is 3-D by a 2-D geometry. In this section, a few points on the strategy are noted.

The main goal of this study is to determine whether the geometry has the potential to be used in a compressor, this will be assessed by determine the pressure difference between the inlet and the outlet. Hence, a velocity will be imposed on the inlet while a reference pressure gauge will be imposed at the outlet. Therefore, the main variable measured will be the inlet static pressure determined by Fluent such that an unsteady periodic flow is obtained.

Furthermore, the motion of the rotor (which is rotational in the 3-D case) is modelled as an upward translation at fixed speed.

3.2.2 Physical Modelling

The different models that were used in this work are presented in the following list:

- **Unsteady simulation.** The problem analyzed is inherently unsteady due to the periodic movement of the rotor. However, it is expected that the solution converges to a so-called "unsteady periodic" pattern, where the solution repeats itself for some quantities. Furthermore, the area weighted average static pressure (arguably the most important flow characteristic in a compressor) and some other variables, are expected to reach a constant value after full convergence to an unsteady periodic solution.
- **No gravity.** Gravity is neglected as it is not a driving force in this setting.
- **Compressible gas.** Air is considered as the fluid circulating in the system and needs to be modelled as a compressible gas due to the nature of a compressor. A gas can only be compressed by such system if it indeed is compressible.
- **Ideal gas.** In order to model air as a compressible gas, the ideal gas law is used as a model. The ideal gas law used by Fluent is given by Equation 3.1 [14], where ρ is the density in kg/m^3 , R is the universal gas constant, M_W is the molecular weight of the gas, T is the temperature, p_{op} is the operating pressure (input) and p is the gauge pressure (computed by Fluent).

$$T \frac{R}{M_W} \rho = p_{op} + p \quad (3.1)$$

This law has limitations due to its main assumption of no inter-molecular interactions, however, it can be considered as a good model for normal temperatures and normal pressures [15]. That is, around atmospheric pressures, which is an expected regime in the situation considered here.

- **Navier-Stokes equations fluid dynamics model.** As all similar CFD softwares, Fluent approximates the solution to the Navier-Stokes equation given by the continuity and momentum balance given by Equations 3.2 [14] and 3.3 [14] respectively.

$$\frac{\partial \rho}{\partial t} + \nabla \cdot (\rho \vec{V}) = S_m \quad (3.2)$$

$$\frac{\partial}{\partial t}(\rho \vec{V}) + \nabla \cdot (\rho \vec{V} \vec{V}) = -\nabla p + \nabla \cdot (\tau^=) + \rho \vec{g} + \vec{F} \quad (3.3)$$

Where \vec{V} is the velocity vector, t is the time variable, S_m is a source of mass, p is the static pressure, $\tau^=$ is the stress tensor, \vec{g} is the gravitational acceleration and \vec{F} represents the external body forces. The $\tau^=$ stress tensor is given by Equation 3.4 [14].

$$\tau^= = \mu_M \left((\nabla \vec{V} + \nabla \vec{V}^T - \frac{2}{3} \nabla \cdot \vec{V} I) \right) \quad (3.4)$$

Where I is the unit tensor and μ_M is the molecular viscosity.

- **Energy model.** As the ideal gas low is used, the energy equations also need to be solved for the temperature field. The energy equation solved by Fluent is given by Equation 3.5 [14]. Where k_{eff} is the effective conductivity, \vec{J}_j is the diffusion flux of species j , e is the internal energy, τ_{eff} is the effective stress sensor.

$$\frac{\partial}{\partial t} \left(\rho(e + \frac{V^2}{2}) \right) + \nabla \cdot (\rho V(h + \frac{V^2}{2})) = \nabla \cdot \left(k_{eff} \nabla T - \sum_j h_j \vec{J}_j + \tau_{eff}^= \cdot \vec{V} \right) + S_h \quad (3.5)$$

- **SST $k - \omega$ turbulence model.** The system analysed is inherently turbulent due to the large Reynolds number that is expected, therefore a turbulence model was selected, as will be detailed in subsection 3.2.4.

The problem considered is inherently unsteady due to the movement of the rotor, therefore, an unsteady simulation was run.

3.2.3 Fluid Properties

As mentioned earlier, air is considered as the circulating fluid in this system. The ideal gas law is used with the properties listed in Table 3.2.

Table 3.2: Fluid properties used in the simulation (default values in Fluent for air)

Property	Value
Specific heat C_p	1006.43 J/(kg K)
Thermal conductivity k	0.0242 W/(m K)
Dynamic viscosity μ	1.7894e-5 kg/(m s)
Molecular weight M_W	28.966 kg/mol

All those variables were taken from the default values showed by Fluent. It is further noted that air is a Newtonian fluid.

3.2.4 Turbulent Flow Calculation

As mentioned earlier, the SST $k - \omega$ turbulence model is used in the simulation, because of its versatility and the absence of needed near-wall treatment. Particularly, it is more accurate and more reliable for a wider class (including airfoils) of flows than the standard BSL models [14]. The model is a RANS 2-equations scheme, tackling the problem through the two model transport equations for TKE are shown below [16].

$$\frac{\partial}{\partial t}(\rho\kappa) + \nabla \cdot (\rho\kappa\mathbf{u}) = \nabla \cdot [\rho\frac{\nu_t}{\sigma_\kappa}\nabla\kappa] + \rho\boldsymbol{\tau} : \nabla\mathbf{u} - \rho\epsilon \quad (3.6)$$

$$\frac{\partial}{\partial t}(\rho\omega) + \nabla \cdot (\rho\omega\mathbf{u}) = \nabla \cdot [\rho\frac{\nu_t}{\sigma_\omega}\nabla\omega] + \rho C_{1\epsilon}\boldsymbol{\tau} : \nabla\mathbf{u}\frac{\omega}{\kappa} - \rho C_{2\epsilon}\frac{\omega^2}{\kappa} \quad (3.7)$$

where:

- κ is the turbulent kinetic energy;
- $\nu_t = \kappa/\omega$ is the turbulent viscosity;
- $\omega = \epsilon/\kappa$ is the turbulent frequency;
- $\sigma_\epsilon, \sigma_\kappa, C_{1\epsilon}, C_{2\epsilon}$ are empirical constants.

3.3 Boundary Conditions, External Forces and Initial Conditions

Next to the geometry, physical modelling and hypotheses, which have been described in the last two subsections, the boundary conditions of the geometry need to be defined as is done in subsection 3.3.1.

In addition to this, the initial conditions of the flow have to be set up in order to successfully run a simulation, which is done in subsection 3.3.2. The geometry is considered not to be influenced by any external forces, so they are not taken into account when setting up the simulation.

3.3.1 Boundary Conditions

Boundary conditions need to be applied for all boundaries of the two surfaces shown in Figure 3.4. The first two boundaries defined are the inlet and the outlet. The inlet is modelled as a velocity inlet in an absolute reference frame with a constant velocity of 35 m/s normal to the boundary and a temperature of 300 K. For the outlet, a pressure outlet was chosen with a gauge pressure of 0 Pa, a temperature of 300.5 K and an absolute backflow reference frame which considers total pressure. By imposing a gauge pressure of 0 Pa, a negative pressure at the inlet is expected to be obtained, which can be used to calculate the pressure difference of the rotor stator stage. The temperature is increased with respect to the inlet, because of the temperature raise caused by the compression.

The boundaries at the top and bottom of the region are defined as periodic boundaries. The two rotors and stators are, as was explained in subsection 3.1.1, only a simplification of a three-dimensional rotor-stator change. As the flow is assumed to be the same around the full radius of the stage, the flow around the two rotors and stators in the geometry will also be the same. This makes it possible to apply translational periodic boundary conditions for all four subsections of the upper and lower boundaries.

For the interfaces between inlet and stator as well as between stator and rotor region, a periodic repeat boundary condition [13] is used. This essentially means that in the part where two interfaces are overlapping, the flow just passes by the interior boundary in the other region. For the two parts of the interface which are not connected with the respectively other region a periodic boundary is used, which translates the flow by the height of the interface, which is for this geometry 340 mm. Indeed, it is valid to assume the flow is the same for this vertical offset, as the flow is the same for all rotor and stator blades around the compressor. The following Figure 3.5 shows all the boundary conditions explained until now and located on the outer domain boundary.

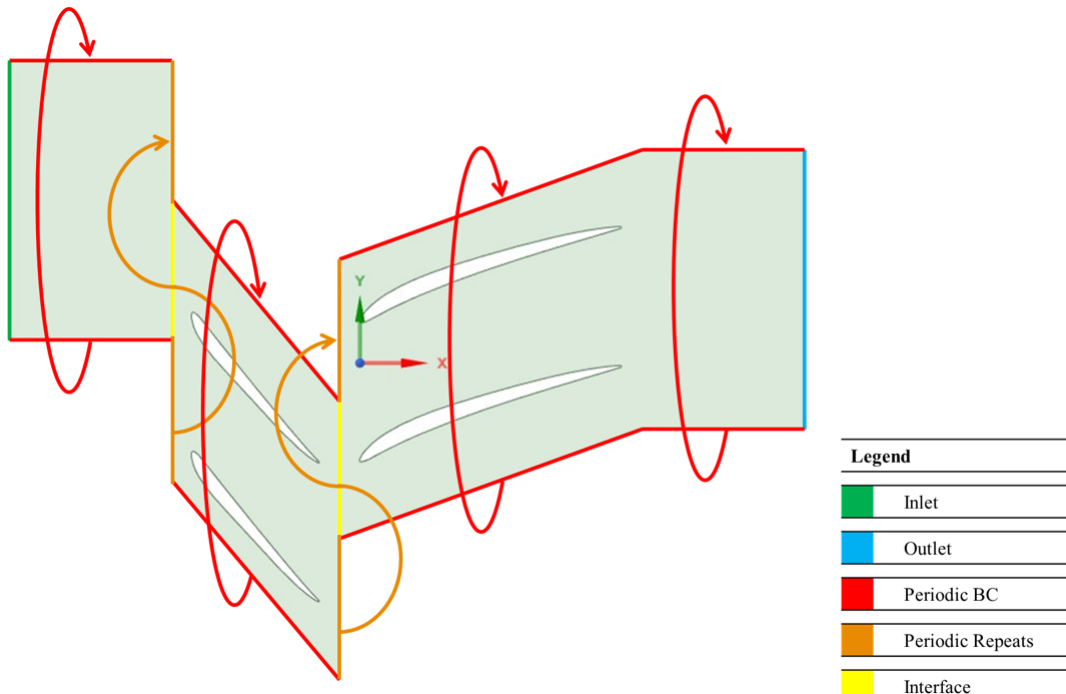


Figure 3.5: Sketch of the different outer domain boundary conditions applied

Finally, for the rotor and stator blades a wall boundary condition is applied. It is specified to have a no slip shear condition and a standard wall-roughness. With this, the boundary conditions have been completely defined for the geometry.

3.3.2 Initial Conditions

The simulation is computationally intensive, showing a need for a proper choice of initial conditions. If those are well-chosen, the startup phase of the unsteady simulation will be shorter, effectively reducing the total computation time required. It was decided to first run a simulation on a coarse mesh with the hybrid initialization tool of Fluent and 0 Pa as initial inlet pressure. This yielded a convergence with an inlet pressure of around $-4,500 \text{ Pa}$, which was used as initial inlet pressure for the final simulation on a finer mesh.

Simulation Details **4**

Having the problem defined in chapter 3, multiple steps described in this chapter are now needed in order to set the solution up. First, the mesh for the geometry needs to be defined in section 4.1, also taking into consideration the possible flow phenomena. In a next step, the numerical methods are chosen in section 4.2. As discussed in section 4.3, a mesh size and domain size convergence study needs to be performed afterwards, in order to obtain the most accurate solution possible.

4.1 Meshing

As described in section 3.1, the geometry is composed of a different surface for the rotor and stator. As the rotor will be considered moving in a vertical direction in the solution, a sliding mesh needs to be used. The mesh will however be done in the same way for the rotor and stator surface, with only minor adjustments for the flow after the stator, in order to have a consistent mesh for the whole domain.

4.1.1 Mesh Type

For meshing, a hybrid unstructured mesh has been chosen. As can be seen in Figure 4.1, an inflation mesh is used around the rotor and stator blades, in order to increase the resolution at the boundary layer, which is particularly important for the solution due to the effects of the airfoils on the flow. The finer inflation mesh is extended behind the stator blades, such that the flow behaviour and especially turbulence in the wake of the airfoils can be observed more accurately. The result can be seen in Figure 4.2. Additional edge sizing was used at the periodic boundaries, the interfaces and around the blades, as will be described in subsection 4.1.3.

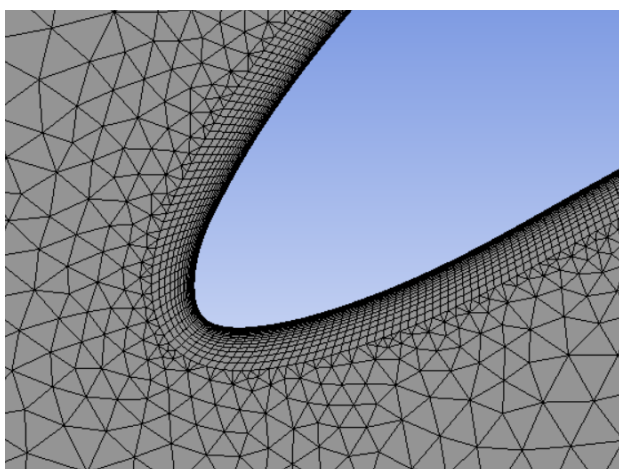


Figure 4.1: Inflation mesh around the airfoils boundary layer

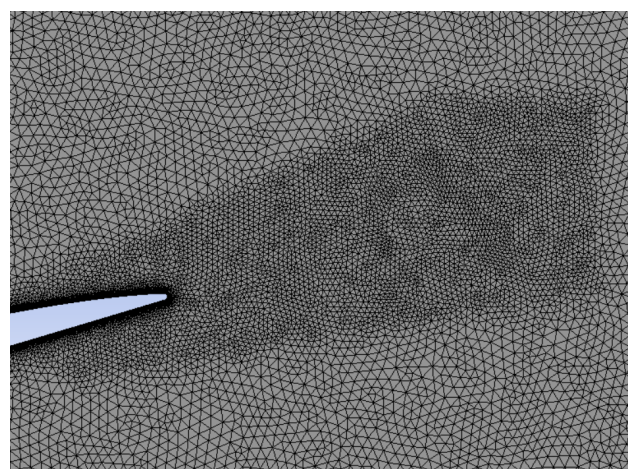


Figure 4.2: Extension inflation mesh at the airfoils wake

4.1.2 Cell Type

Different cell types are chosen for the mesh. In general, the mesh is composed of triangular mesh elements. They allow to connect the different mesh types as well as the boundaries in the cleanest way. Additionally, they can be used easily to obtain local mesh refinement, which is used in locations with specific flow phenomena as described in subsection 4.1.1.

For the inflation layer around the airfoil as well as for the extension at the wake of the airfoil, quadrilateral mesh cells are used. They allow refining the mesh parallel to the airfoil surface as well as parallel to the flow in the airfoils wake in a straightforward manner. In addition, the connection between them and the rest of the mesh is no problem due to the unstructured nature of the triangular mesh.

4.1.3 Size and Number of Cells

As was shown already in Figure 4.2, the mesh was refined behind the trailing edge of the stator blades, where particularly important flow phenomena are expected. A factor of 0.5 was used for the refinement compared to the overall mesh cell size. If for example the general mesh element size is equal to 5 mm, the element size for the refinement region is in consequence 2.5 mm.

Additional mesh refinement was introduced at all periodic boundaries, in order to make sure the same number of elements is present on both periodic surfaces. For the edge sizing used, the same refinement factor of 0.5 has been chosen as for the previously mentioned refinement region at the stator trailing edges. Furthermore, the mesh was also refined at the interfaces in order to ensure the flow characteristics are passed from the rotor to stator region in the most accurate way possible. Additionally, due to the proximity of the interface to the rotor and stator blades (whose edges were also refined, as will be described next), this allows to have a relatively fine mesh between rotor and stator and consequently more accurate results in this critical region for the flow. Again, a mesh refinement factor of 0.5 was used at the interfaces.

Finally, the mesh around the boundaries of rotor and stator blades needed to be defined. This was done as described earlier with an inflation layer. For this, an inflation layer with a maximum number of 20 layers has been chosen. The first layer height was set to be equal to 0.01mm. In order to firstly have a finer mesh also around the inflation layer, secondly to limit the difference in size between the mesh cells of the inflation layer and the triangular cells around them and thirdly in order to improve orthogonality of the mesh cells in the inflation layer, edge sizing was also introduced around the blade edges. For this, a factor of 0.1 compared to the general mesh element size has been found to sufficiently increase the lowest orthogonality results of the mesh. This means that for a mesh element size of for example 5mm, an edge sizing of 0.5mm was imposed at the blade boundaries. A sketch of all applied refinement is shown in Figure 4.3.

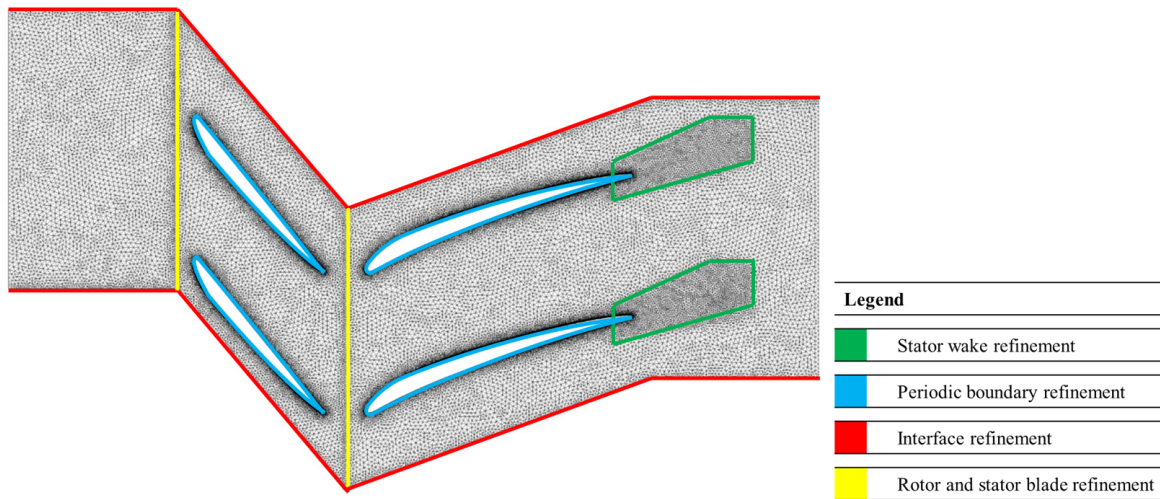


Figure 4.3: Sketch of all refinement applied on the mesh

4.1.4 Final Mesh

The final mesh has been obtained using a convergence study, which is explained more in detail in section 4.3. A global mesh element size of 3.3333mm has been chosen for the final mesh. The same refinements as described in subsection 4.1.3 were applied to this mesh. This leads to the element or edge sizes shown in Table 4.1. The mesh obtained is shown in figure 4.4. It has a total of 253042 mesh cells and of 201044 nodes.

Table 4.1: Refined regions and boundaries and their element or edge size.

Regions and boundaries	Element or edge size [mm]
Stator wake region	1.6666
Periodic boundaries	1.6666
Interfaces	1.6666
Rotor and stator blade walls	0.3333

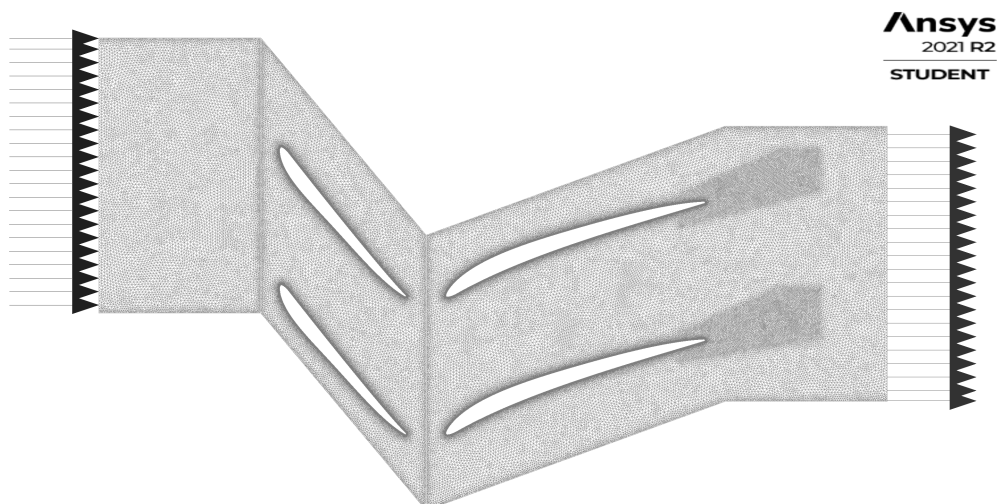


Figure 4.4: Final mesh used in this study

In order to analyse the performance of the mesh, its quality metrics need to be analysed. The first metric analysed is the orthogonality of the mesh elements. As can be seen, in Figure 4.5, most of the elements have an orthogonality close to 1. In fact, the average orthogonality of the mesh is 0.97398 and the minimum orthogonality 0.37953. The orthogonality of the mesh is therefore very good, as orthogonality values close to 0, which could lead to numerically less accurate results [16], are largely avoided. A second metric which can be looked at is the skewness of the mesh element. In this case, values close to 1 need to be avoided, in order to ease convergence of the solution [16]. As can be seen in Figure 4.6, this is successfully the case for the obtained mesh. An average skewness of 0.06388 and a maximum skewness of 0.85258 additionally confirm this requirement to be met.

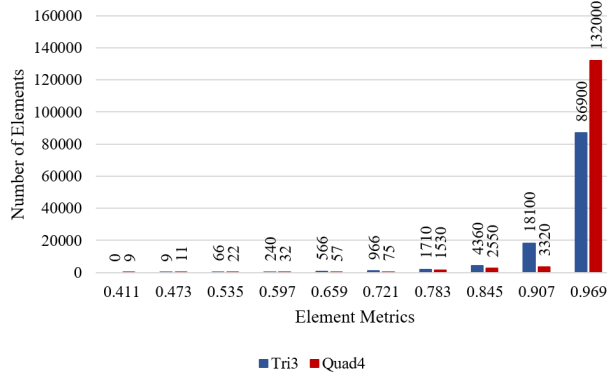


Figure 4.5: Orthogonality metrics of the final mesh used in this study

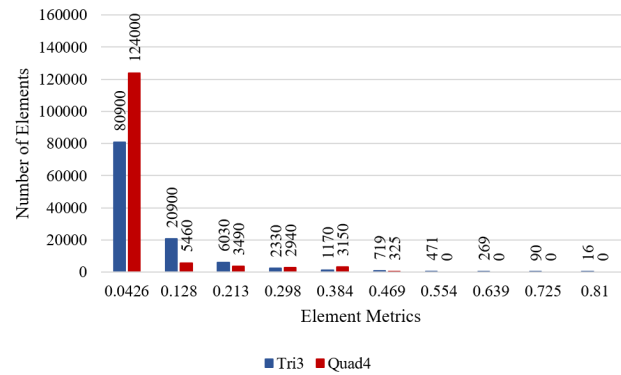


Figure 4.6: Skewness metrics of the final mesh used in this study

Another mesh metrics which can be looked at is the aspect ratio of the elements. At best, this should be close to 1 [16]. However, the triangular and quadrilateral elements need to be analyzed separately. As can be seen in Figure 4.7, for the triangular elements the aspect ratio is close to 1 for all cells and the requirement is therefore met. For the quadrilateral elements, much larger results up to aspect ratios of 38.53 are obtained. However, as those elements are only used at the boundary layer of the airfoil, where the gradients are mostly in the stretched direction of the elements, this is perfectly fine for the mesh. Regarding the smoothness of the mesh, this can be analyzed for the boundary layer of rotor and stator blades, where an inflation was applied. A growth rate of 1.2 was chosen for the inflation layer, which allows a smooth mesh around the blades without prompt changes.

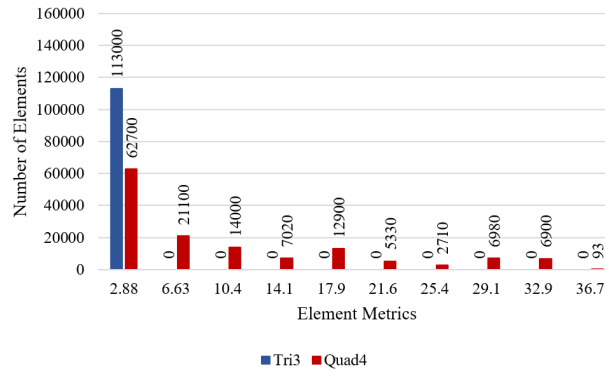


Figure 4.7: Aspect ratio metrics of the final mesh used in this study

4.2 Numerical Methods

The right choice of the numerical methods applied during the simulation is fundamental to obtain a realistic and accurate result. Furthermore, numerical results are plausible only if the chosen method has properties of conservativeness, boundedness and transportiveness.

4.2.1 Spatial Discretization Method

In order to discretize the domain Fluent uses the Finite Volume Method (FVM). The domain is divided into a set of control volumes (mesh) and a node is assigned to each of them. The unknown variable (Φ) is then discretized with nodal values and each term of the governing equations is approximated as a function of nodal values. This converts the system of partial differential equations 4.1 in an algebraic equation system 4.2 [16].

$$\frac{\partial}{\partial t} \int_V \rho \Phi dV + \int_A \rho \Phi \mathbf{u} \cdot \mathbf{n} dA = \int_A \Gamma \nabla \Phi \cdot \mathbf{n} dA + \int_V S dV \quad (4.1)$$

$$\mathbf{A}(\Phi) = 0 \quad (4.2)$$

First order upwind differencing (UD) is chosen for the spatial discretization. The method performs a constant interpolation, considering the upstream nodes, relatively to the flow direction. The method is bounded because it respects the Scarborough criterion and the coefficients of the algebraic equations in the system have the same sign. It is transportive, because the influence of the neighbouring nodes is not symmetric by construction and it is conservative. Given the fact that the simulation is computationally heavy because of the sliding mesh, unsteadiness and obliged choice of very small size of the time step, a tradeoff between time and accuracy of the results has to be taken into account. For the scope of the present report, a first order accuracy was considered to be a proper compromise.

4.2.2 Type of Simulation and Solver

The case study taken into consideration is dynamic, because of the rotor periodic motion, therefore the simulation is unsteady. Furthermore, the solver is density based, recommended when treating compressible flows, and coupled, meaning that it solves mass, momentum and energy equations simultaneously; the equations for other quantities are then computed afterwards. For every iteration loop, the governing equations are linearized, and the linear system is solved [13]. This implies that the simulations are computationally more expensive, but can give a higher accuracy. The solver gives the possibility to choose between coupled implicit or explicit methods, influencing the way in which the non-linear equations are converted into linear ones. An explicit method is preferred, because of lower computational cost. Using this method, the unknowns appear in only one equation of the linearized system, without depending on the others; therefore, every equation can be solved to give the unknown quantity.

In order to have a deep and comprehensive study of the presented engineering problem, solutions for multiple variables are presented. The following quantities are investigated:

- *Pressure, Velocity* → In an axial compressor the quantities of greatest interest are pressure and velocity. The analysis of the evolution of these fields over space and time through the stage gives several insights on the possible applications and purposes (i.e. compression ratio, mechanical stresses etc.);

- *Density* → The variation of density is investigated, in order to understand what are the parameters of the flow along the studied stage and before entering the next one. Indeed, subsequent stages have a reduction in section and the increase in density has to be coupled with it;
- *Temperature* → Temperature inside the unit is also analyzed, to predict which are the thermal stresses developed inside the machine and to monitor that the maximum limit tolerated by the materials is not overcome. This gives also insights on the choice of the cooling system and the material itself, that can be adapted to reach higher temperatures, and thus a higher compression ratio;
- *Turbulent kinetic energy (TKE)* → The kinetic energy dissipated by the vortices is important to understand the influence of turbulence on wake dispersion. To compute the TKE the $k - \omega$ model is used. The two model transport equations for TKE are eq. 3.6 and 3.7.

4.2.3 Solution Options

The hybrid initialization is used to initialize the field. This method accelerates the overall computation, giving a better initial guess for the flow variables if compared with the standard one, because it solves the Laplace equation to output a velocity field conformal with complex geometries and a pressure field that connects smoothly high and low pressure values along the field [14]. In order to have faster convergence, sensitivity analysis is performed to verify the most suitable initial value for inlet pressure.

Given the fact that the simulation is unsteady, a suitable temporal discretization scheme has to be implemented. The unknowns of the problem depend on both time and space $\Phi(x, t)$, introducing the need to deal with a system of PDE (Equation 4.3 [16]). The temporal discretization converts it to a system of ODE (Equation 4.4).

$$\frac{\partial}{\partial t}(\rho\Phi) + \nabla \cdot \rho\Phi\mathbf{u} = \nabla \cdot \Gamma\nabla\Phi + S \quad (4.3) \qquad \frac{\partial}{\partial t}(\Phi) = \mathbf{A}(\Phi) \quad (4.4)$$

To discretize the equations over time, an implicit 1st order scheme (Backward Euler) is implemented, because of its unconditional stability. The scheme computes Φ at each time step as shown below [16].

$$\Phi^{n+1} = \Phi^n + \Delta t(\theta f^{n+1} + (1 - \theta)f^n) \quad \theta = 1 \quad (4.5)$$

For choosing the time step size, the Courant-Friedrichs-Lewis (CFL) condition [16] has to be taken into account.

$$CFL = \frac{u\Delta t}{\Delta x} \quad (4.6)$$

This value represents the 'amount' of flow u that is crossing a cell in the computational mesh Δx in a certain time step Δt . The CFL number cannot be higher than one in explicit Eulerian methods, otherwise the information propagates through more than one cell at each time step. For the chosen method (Implicit Euler), the condition can be relaxed thanks to the fact that is unconditionally stable, giving more freedom in the choice of the time step size.

The time step size has to be chosen depending on the geometrical dimensions and the motion of the rotor, in order to have a suitable number of time steps between two subsequent blades. Given that the rotor translational velocity is 100 m/s and the distance between consecutive blades is 17 mm, the

time required for the rotor to cover the distance between the stator blades is 1.7 ms. Therefore, a suitable time step is $\Delta t = 10^{-4}$, guaranteeing 17 time steps between consecutive blades and ensuring a reasonable computational cost. The total time interval needed to reach a constant compression ratio after the initial transient start-up, considering $\pm 5\%$ on the amplitude of the oscillations, is around 0.14 s (1400 time steps).

4.3 Mesh Size Convergence Study

In this section, a mesh convergence study will be carried for the geometry and mesh shown in Sections 3.1 and 4.1. Due to the time constraints, this will be done by considering the case of a frozen rotor stator stage, which comes back to the steady-state solution of the problem considered. This is deemed to be a valid approach as the large velocity gradients are expected to be found in the same regions for both the steady and unsteady case. In both cases, the velocity changes drastically when it encounters the airfoils, and it is expected that similar flow patterns with the unsteady simulation can be found at the interface between the airfoil rows and after the stator. However, this assumption will require careful checks once the solution in both a steady and unsteady case is obtained.

Furthermore, the domain size of the simulation will not be investigated, as the geometry should stay close to reality. Indeed, the geometry considered should be seen only as one part of a series of stages. This means that the outlet of the simulation is kept quite close to the stator end, as the flow behaviour further away would be affected by the next stage. This also means the flow is expected to still have some relatively large variations in its quantities while reaching the outlet.

First, some criteria need to be selected in order to assess convergence. In this case, both the static pressure inlet and velocity outlet will be used, as they are both critical variables of interest to the design (especially the former). Determining whether convergence is reached comes back to assessing whether coarser and finer meshes tend to approach the same values of the selected criteria variables. Therefore, the profiles of both variables will be compared for different meshes.

The convergence study will be presented as follows: First, the meshes used in the convergence study are presented in subsection 4.3.1. Consequently, for those meshes and especially the coarsest and finest one, the results are analyzed in subsection 4.3.2. The relative error for the different meshes is then estimated in subsection 4.3.3 and the final mesh is chosen in subsection 4.3.4. Finally, the inflation layer characteristics are verified by analysing $Y+$ in subsection 4.3.5.

4.3.1 Presentation of the Different Meshes

In total, seven different meshes will be considered in this convergence study. Each mesh will be obtained by considering a constant refinement or coarsening factor of 1.5 to the general mesh element size. As described in section 4.1, the mesh is additionally refined in some specific regions and at some boundaries of the domain with respect to the global mesh. In order to keep the same refinement factors of some regions for all meshes used in the convergence study, a parameter was used with the global mesh element size as input parameter. All the regions and edges concerned and their refinement with respect to the overall mesh size are given in Table 4.2. A visualization has been shown in Figure 4.3.

Table 4.2: Refined regions and boundaries with respect to the overall mesh element size

Regions and boundaries	Refinement factor k
Stator wake region	0.5
Periodic boundaries	0.5
Interfaces	0.5
Rotor and stator blade walls	0.1

This means that for any mesh considered with global mesh element $x m$, the mesh size in those regions is $k \cdot x m$. The relevant information of each mesh is given in Table 4.3.

Table 4.3: Properties of meshes used in the convergence study

# Mesh	Global Element Size [mm]	Nb Cells	Nb Nodes
1	25.3125	27,180	22,444
2	16.8750	43,844	36,292
3	11.2500	68,078	56,087
4	7.5000	103,432	86,029
5	5.0000	158,688	128,536
6	3.3333	253,042	201,044
7	2.2222	420,620	322,157

Note that a mesh refinement factor of 1.5 on the global mesh element size was used to generate the seven meshes. The coarsest and the finest mesh obtained, which will also be used for the analysis in subsection 4.3.2, are shown in Figure 4.8 and Figure 4.9.

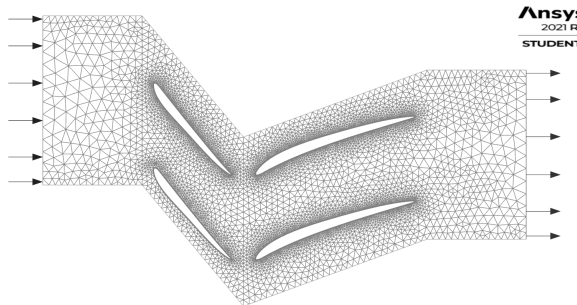


Figure 4.8: Coarsest mesh of the convergence study (global element size of 25.3125 mm)

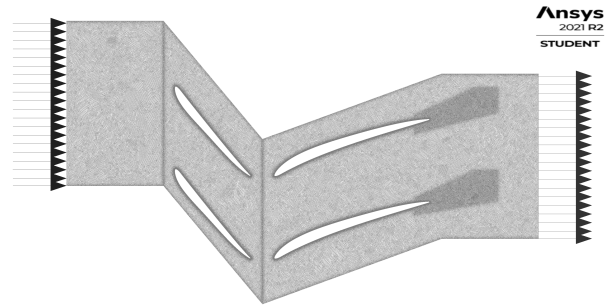


Figure 4.9: Finest mesh of the convergence study (global element size of 2.2222 mm)

4.3.2 Frozen Rotor Stator Simulation

A few notes need to be mentioned, concerning the simulation setup of the frozen rotor-stator case as it has some differences with the transient simulation that is the core of this work (and will be analyzed in the chapter 5). Mainly, the simulation is run as a steady simulation and a pressure based solver was used to ensure faster convergence. The latter is made possible by the fact that smaller Mach numbers are predominant in the frozen rotor stator case. Furthermore, a standard initialisation with the Fluent default values was used instead of the hybrid option to ensure no effect of the initial condition on the final convergence of the steady simulation (as hybrid could obtain slightly different initialisation guesses on the different meshes).

4.3.2.1 Results on the Coarsest Mesh

First, the results on the coarsest mesh (global element size of 25.3125 mm) are shown. For this mesh, the area-weighted average pressure difference between inlet and outlet converged to a value of 7873.966 Pa and the area-weighted average velocity at outlet to a value of 45.474 m/s. The corresponding pressure and velocity magnitude fields can be seen in Figure 4.10 and Figure 4.11: As can be observed, the overall flow can already be observed quite accurately at this mesh, even if it is still quite coarse, especially far away from the airfoils, in the inlet and outlet region.

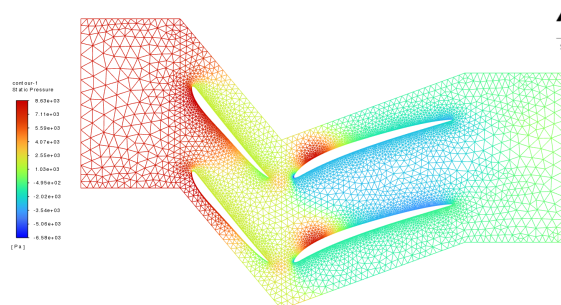


Figure 4.10: Static pressure on the coarsest mesh in the convergence study (global element size of 25.3125 mm)

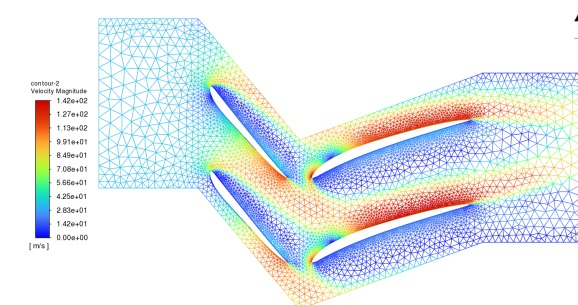


Figure 4.11: Velocity magnitude on the coarsest mesh in the convergence study (global element size of 25.3125 mm)

Specific regions are observed, where refinement might be useful: As can be seen in both the pressure and the velocity flow fields, especially the boundaries around rotor and stator blades should be refined. Another interesting region of refinement is the region between rotor and stator, where the flow direction changes. Lastly, the region behind the stator shows interesting flow behavior, which might be interesting to analyze. Those regions consequently match with the refinement regions, which were used for meshing as described in section 4.1.

4.3.2.2 Results on the Finest Mesh

In a second step, the results on the finest mesh (global element size of 2.2222 mm) are shown. Compared to the coarsest mesh, the area-weighted average pressure difference between inlet and outlet is 16.7% higher with a converged result of 9186.011 Pa. The difference of the area-weighted average velocity at outlet is less important: With a velocity of 47.002 m/s, the converged result is only 3.4% higher for the fine than for the coarse mesh. As can be seen in Figure 4.12 and Figure 4.13, the flow behavior looks very similar to the results obtained on the coarsest mesh. However, it can be observed, that especially the changes in velocity at the stator leading edge are displayed much more accurately on this finer mesh than on the coarser meshes shown in subsubsection 4.3.2.1. It is therefore indeed helpful to refine the flow around the blades, as was described in section 4.1.

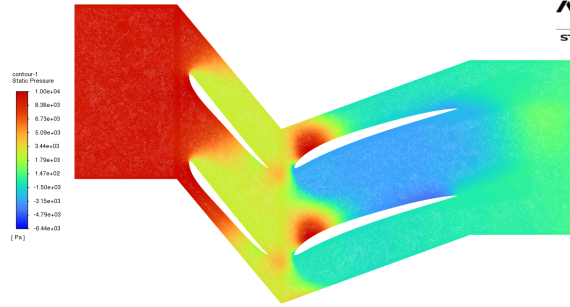


Figure 4.12: Static pressure on the finest mesh in the convergence study (global element size of 2.2222 mm)

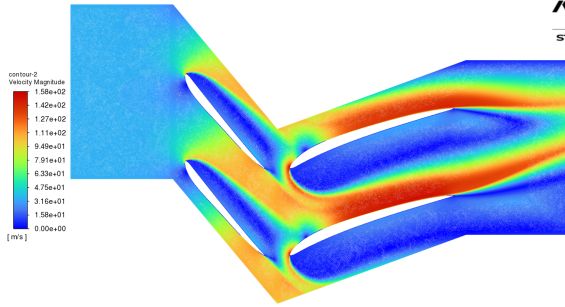


Figure 4.13: Velocity magnitude on the finest mesh in the convergence study (global element size of 2.2222 mm)

4.3.2.3 Variation of Results from the Coarsest to the Finest Mesh

For every convergence study step, the area-weighted average pressure difference between the inlet and outlet as well as the area-weighted average velocity at the outlet were stored. The results for all steps could be plotted in Figure 4.14 and Figure 4.15. As can be seen in the graphs, especially the result for the pressure difference is clearly converging for every step. For the velocity at the outlet, convergence can't be observed as easily. In consequence, the incremental variation will be analyzed.

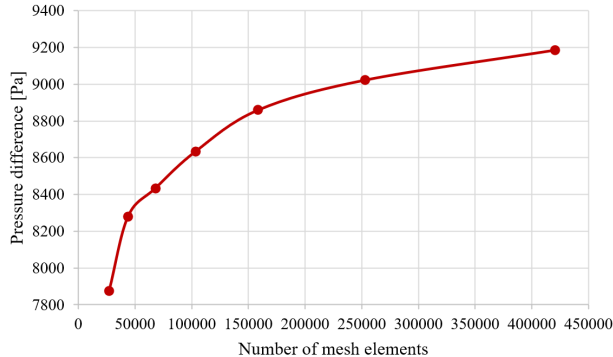


Figure 4.14: Evolution of the pressure difference from the coarsest to the finest mesh

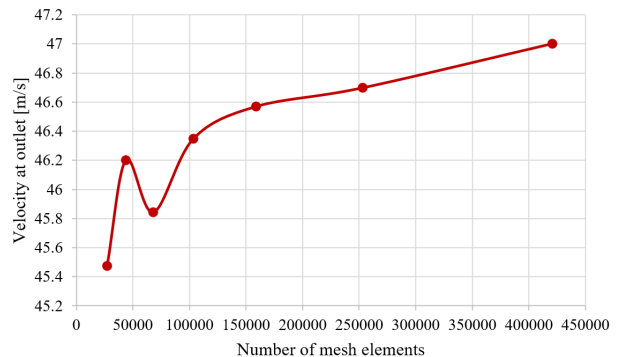


Figure 4.15: Evolution of the velocity at outlet from the coarsest to the finest mesh

The incremental variation for the pressure difference and velocity at outlet can be seen in Figure 4.16 and Figure 4.17. An incremental variation of maximum 2% was considered to be acceptable. For the pressure difference, which is considered to be the most important criteria, it can be observed that the incremental variation is rapidly decreasing from the first step and settles then at a value slightly smaller than 2%. For the velocity at the outlet, the incremental variation for the velocity at the outlet is in general decreasing as well, but it seems to be oscillating and it is more difficult to observe a clear trend as for the pressure difference. For the last 3 steps, the incremental variation is smaller than 1%, which shows that the differences are in general quite small and already acceptable.

Based on the results Figures 4.14, 4.13, 4.16 and 4.17, it can be argued that using a few additional finer mesh sizes would be better to ensure convergence with more confidence. However, the maximum number of elements was already reached already within this convergence study.

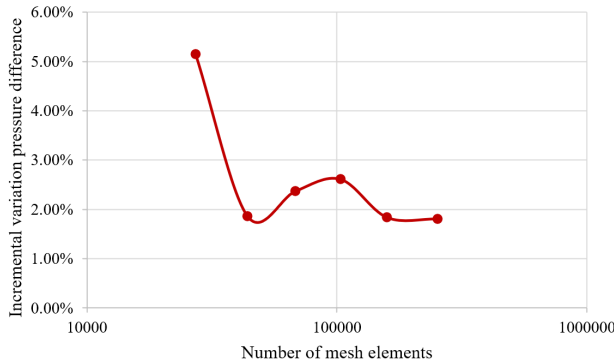


Figure 4.16: Incremental variation of the pressure difference from the coarsest to the finest mesh

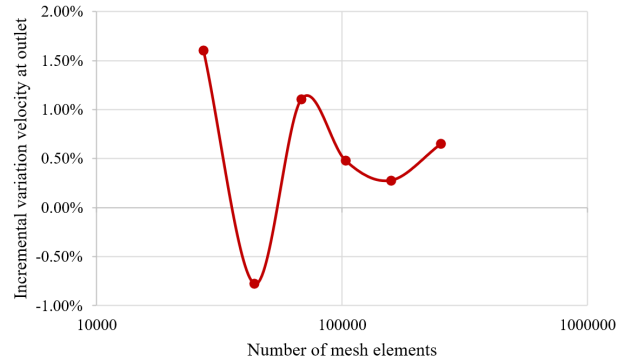


Figure 4.17: Incremental variation of the velocity at outlet from the coarsest to the finest mesh

4.3.3 Estimation of the Relative Error

In a next step, an error estimate of the results obtained in subsubsection 4.3.2.3 needs to be made. A threshold of 2% has been chosen for the final mesh. The error estimate is performed by calculating the relative error for both pressure difference and velocity at the outlet for every mesh with respect to the finest mesh available. The results of this analysis can be seen in Figure 4.18 and Figure 4.19. For the pressure difference, it can be observed that the slope of the relative error graph is decreasing for from the coarser to the finer meshes. The threshold is met only for the second-last step. As for the velocity at the outlet, the decrease of the relative error is less apparent, but the relative error threshold is already met for the second as well as for the last 4 meshes of the convergence study.

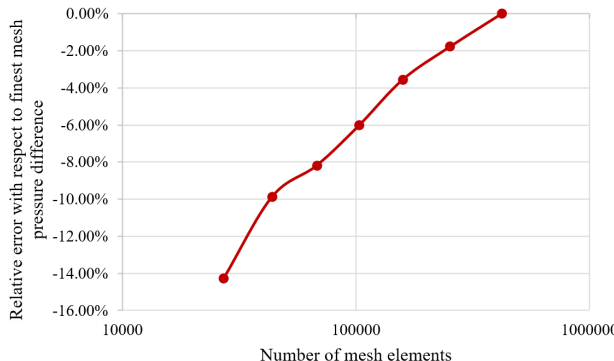


Figure 4.18: Variation of the relative error for the pressure difference

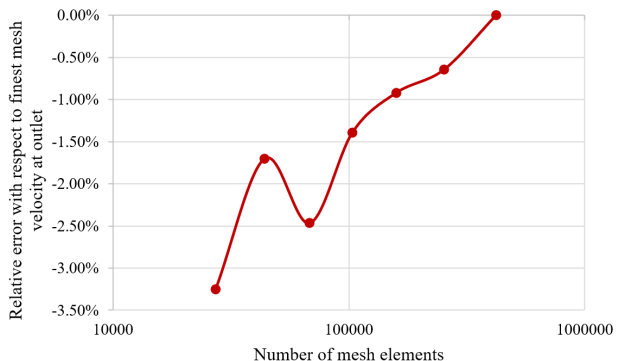


Figure 4.19: Variation of the relative error for the velocity at outlet

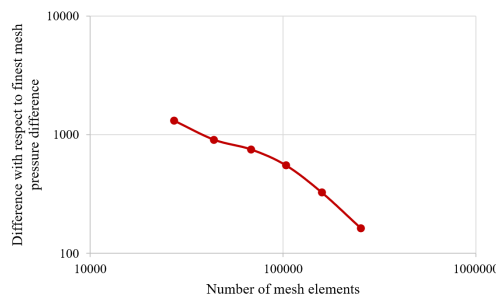


Figure 4.20: Difference with respect to finest mesh for the pressure difference

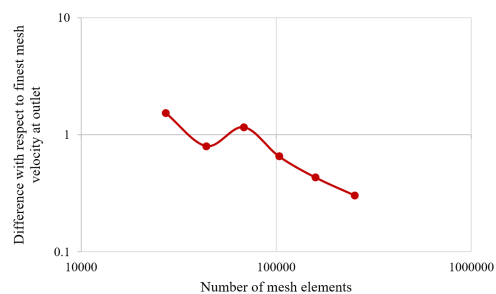


Figure 4.21: Difference with respect to finest mesh for the velocity at outlet

Considering Figures 4.20 and 4.21, it is clear that the convergence is reaching the asymptotic region, showing a slope approximately equal to the solver order on the loglog plots. It can be seen that the first data points lie in a region of oscillation, meaning that this data is not reliable and should not be used under any circumstance. However, the last three seem to have reached the convergence region and the finest or second finest can be used with a certain level of confidence about their reliability.

Another available method to estimate the discretization error is a Richardson extrapolation [16]. This can be used, if a uniform refinement factor is applied for the whole domain. However, in the case of the mesh used, the layer heights of the inflation layer are constant for all meshes used in the convergence study. In consequence, the refinement factor is not uniformly applied for the complete mesh. Therefore the Richardson extrapolation was not considered to be fully valid for this study.

4.3.4 Choice of the Mesh

As a requirement for the mesh chosen for this study we imposed a relative error smaller than 2% compared to the finest mesh of the convergence study as well as an incremental variation less than 2%. As can be seen in Figure 4.19, the first requirement is met for all meshes with a global element size smaller or equal than 16.8750 mm for the velocity at the outlet, but for the pressure difference this requirement is only met for the meshes with a global element size of 3.3333 and 2.2222 mm, as can be seen in Figure 4.18. The second requirement is again only met for the last two meshes if both the pressure difference in Figure 4.16 and velocity at the outlet in Figure 4.17 are taken into account. Consequently, the coarsest of the possible meshes was chosen, in order to limit computational time as much as possible for the unsteady simulations. As a result, mesh 6 with a global element size of 3.3333 mm was chosen. More details on this mesh and its quality metrics can be found in subsection 4.1.4.

4.3.5 Validation of Y+

In a last step, due to the possible turbulent nature of the flow around the blades, Y_+ of the first cell height around the blades needs to be verified. This will be done both for the steady and unsteady simulation with a mesh of a global element size of 3.3333 mm, which was the mesh chosen after the convergence study. In order to be able to use wall resolution, Y_+ should in general be lower than 3, in order to still be in the viscous sublayer. As can be observed in Figure 4.22 and Figure 4.23, for both the steady and unsteady simulation, only at the leading edge Y_+ is slightly higher than 3 but otherwise it is lower than this threshold. As the value of 3 for Y_+ is not a strict limit and only very few cells have a value of Y_+ slightly higher than 3, the mesh around the blades and wall resolution are valid for correctly obtaining turbulence.

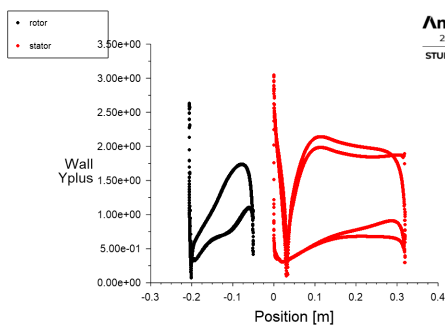


Figure 4.22: Y_+ around the blades in the steady simulation

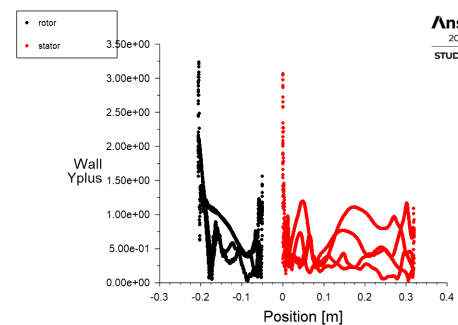


Figure 4.23: Y_+ around the blades in the unsteady simulation

Results and Discussion

5

In this chapter, the results of the simulation are presented. First, the setup of the simulation will be presented in section 5.1, this will be followed by a discussion of the convergence of the simulation to a periodic solution in section 5.2. Then, general flow characteristics of the obtained solution will be presented in section 5.3 and section 5.4 will analyse the flow around the airfoils. Finally, a comparison with the flow around a frozen rotor-stator configuration will be presented in section 5.5.

5.1 Setup Summary

In this section, a short summary of the setup of the solution as discussed in the previous chapter is given. The main elements of the setup within Fluent are the following:

- The Density-Based solver type is used for the transient 2-D simulation. All the first order solvers are used, explicit in space and implicit in time. Furthermore, double precision is used.
- The fluid is taken to be air and is modelled by the ideal gas law with the constant fluid properties given in Table 3.2.
- The solution to the full Navier-Stokes and energy equations for an incompressible fluid is approximated. Additionally, the $k - \omega$ turbulence model is used.
- The BCs are periodic on the upper and lower parts of the domain, a velocity inlet of 35 m/s with initial gauge pressure of $-4,500\text{ Pa}$, and a pressure outlet of 0 Pa gauge pressure. Furthermore, an operating pressure of 101325 Pa is used.
- The movement of the rotor is modelled using a sliding mesh with an upward velocity going at 100 m/s .

As the gauge pressure is fixed at the outlet, the gauge pressure at the inlet is used to assess whether the system is able to compress the fluid going through it. The solution presented in the following was obtained using a global mesh size of 3.333 mm after 1,660 time steps of 10^{-4} s , which is equivalent to around 50 simulation cycles. The solver was initialised using the hybrid option.

5.2 Solution Convergence

In order to establish the characteristic parameters of the system (e.g. compression ratio, velocity field etc.), the unsteady simulation is carried out. As reference criteria for the convergence, the main parameters of the axial compressor are considered: pressure and velocity. To determine the exact pressure difference between inlet and outlet, the gauge pressure at outlet is imposed to 0 Pa ; thus, the inlet pressure will be negative, meaning that the machine is actually increasing the pressure of the fluid. After an initial unstable transient behaviour, shown in Fig. 5.1, it can be observed that the

unsteady periodic state is reached after approximately 0.14 s (1400 time steps), taking into account a variation of $\pm 5\%$ on the oscillations. The pressure at inlet is equal to -4455 Pa (Fig. 5.1), resulting in a compression ratio of 1.045. The outlet velocity stabilizes to a value of 39.2 m/s. The work given to the machine is used to increase the pressure energy and kinetic energy of the fluid.

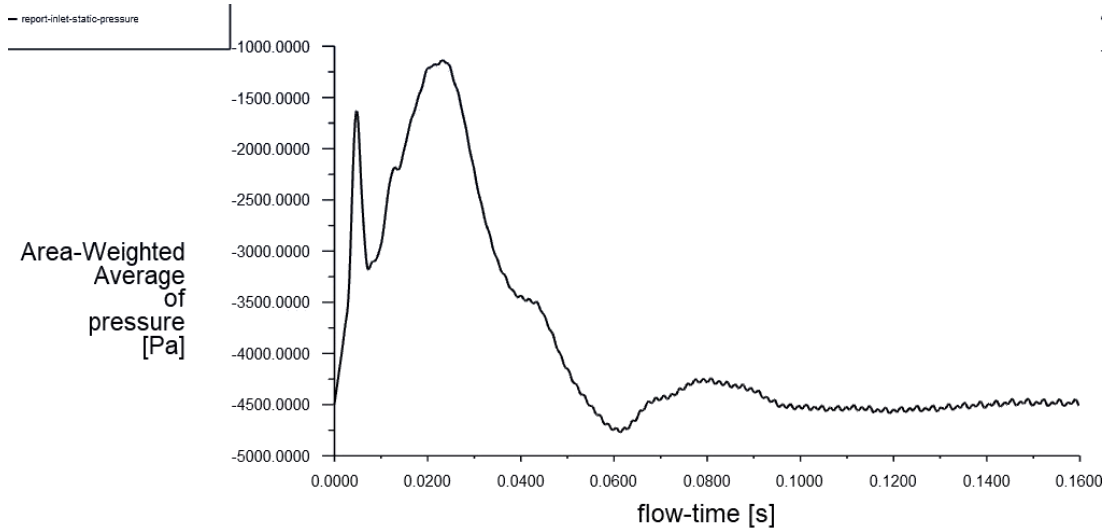


Figure 5.1: Inlet static pressure

In Fig. 5.2, the scaled residuals are shown. The periodic evolution of the residuals over time, typical of unsteady simulations, can be noticed. The values of the residuals are low as the simulation has reached convergence. In particular, the TKE and turbulent frequency residuals are of an order of magnitude of 10^{-4} , x- and y- velocity are respectively 10^{-3} and 10^{-2} , while energy is 10^{-1} .

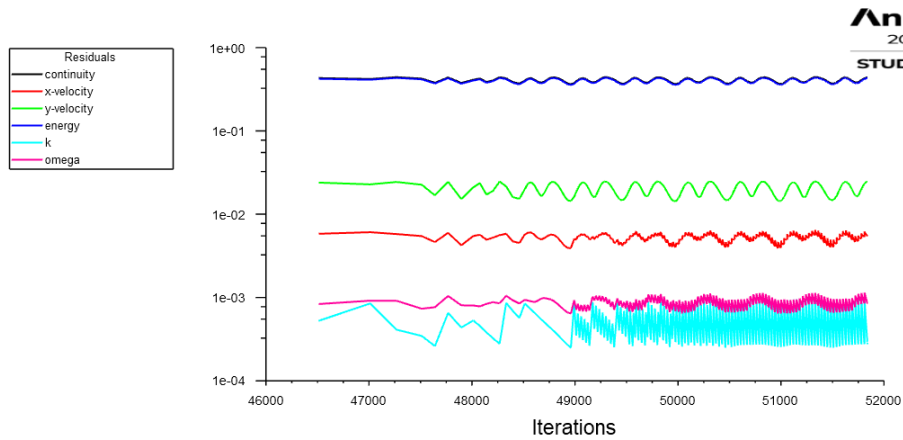


Figure 5.2: Scaled residuals over time

The mass balance has to be verified, to understand if the system respects the conservation of mass (3.2). Given the fact that the simulation is unsteady periodic, the net mass between inlet and outlet cannot be computed at a single instant in time, otherwise it will result in an imbalance. It has to be taken into account that, having imposed a velocity inlet as a boundary condition, the mass flow rate can vary in time. Therefore, to calculate it, the difference of the average of the mass flow rate at inlet and outlet is performed. In Fig. 5.3 and 5.4, the periodic evolution of mass flow rate over time is displayed. Averaging the period and subtracting the outlet one to the inlet one, around -1 kg/s is obtained. This is due to the fact that there is some flow recirculation across inlet/outlet during the

initial transient; the problem could be solved making the simulation run for a higher number of cycles or adding a very large outlet extension to the CAD. The first possibility would imply a very high computational cost, given that to run 1660 steps (total simulation time), the software needed around 8 hours; the second suggestion has not been implemented because of time constraints.

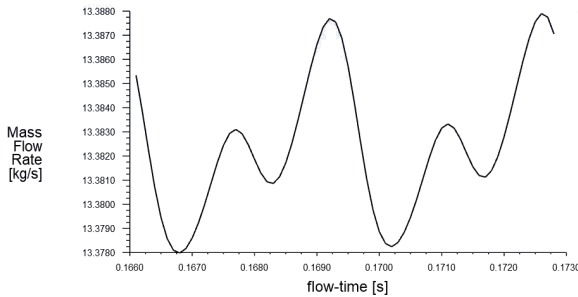


Figure 5.3: Inlet mass flow rate

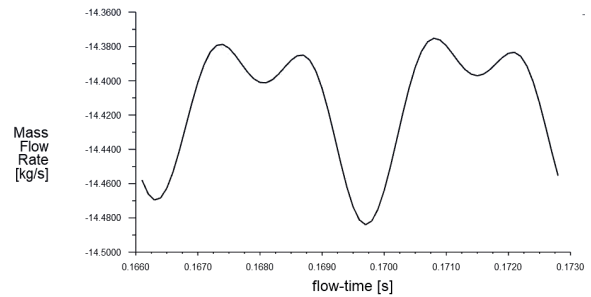


Figure 5.4: Outlet mass flow rate

5.3 General Flow Characteristics

In this section, the main flow characteristics will be described, with the goal to better understand the flow behaviour over a dynamic rotor-stator stage. The main question to answer concerns how a rotor-stator stage is able to compress the incoming flow. But first, the relevant dimensionless numbers are noted to be the Reynolds and the Mach number [17]. The Reynolds number of the system is computed considering the chord of the larger airfoil L as characteristic length and the average velocity u at outer stator blade as characteristic velocity. The value shows that the regime is turbulent and that inertial forces prevail over viscous forces. The maximum Mach number across the system is 0.33, computed using the maximum flow velocity along the compressor, implying a subsonic flow. Given the fact that it is larger than 0.3, the compressible equations have to be used, because compressibility effects are not negligible.

$$Re = \frac{uL}{\nu} \simeq 8 \cdot 10^5 \quad Mach_{max} = \frac{u_{max}}{a} = 0.33 \quad (5.1)$$

where a is the speed of sound in the medium.

Diving into the results, the static pressure in the domain considered in given by Figure 5.5. Note that in the following, the static pressure mentioned is actually the gauge static pressure (measured with respect to the operating pressure). It is then directly clear that the geometry considered is able to compress the fluid in the given setting. As mentioned earlier, the pressure increase over the system is about 4,455 Pa, however, the static pressure with respect to the inlet reached a peak at 6,595 Pa at the leading edge of the rotors. On the other hand, the minimum static pressure was observed at on the leading edge on the lower side of the rotor airfoil, with a pressure drop of 8,345 Pa with respect to the inlet values.

It is important to remember that the contour shown is only a snapshot of the flow characteristics at a moment in time. In reality, the rotor blades are moving up with a velocity of 100 m/s, explaining why suction occurs on the lower side. In order to better understand the flow behaviour at the interface between the rotor and stator, the range of the colour map is now limited to exclude the global minimum. This is shown in Figure 5.6.

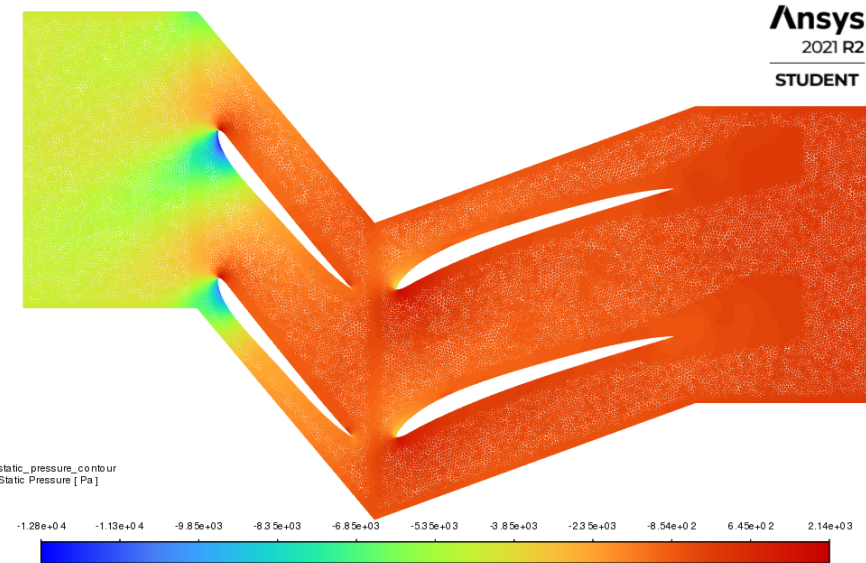


Figure 5.5: Static pressure contours in the domain at $t = 0.166\text{ s}$

In Figure 5.6, it is seen that the pressure increases significantly on the lower side of the stator. Furthermore, looking at the velocity vector directions, it is clear that the airfoil is directed towards the leading edge of the stator. The pressure rises in the system as the airflow encounters the stator as an obstacle, this can be explained by approximating the fluid and considering Bernoulli. Assuming that the total pressure along a streamline remains constant, most of the dynamic pressure is traded for static pressure, hence a static pressure increase.

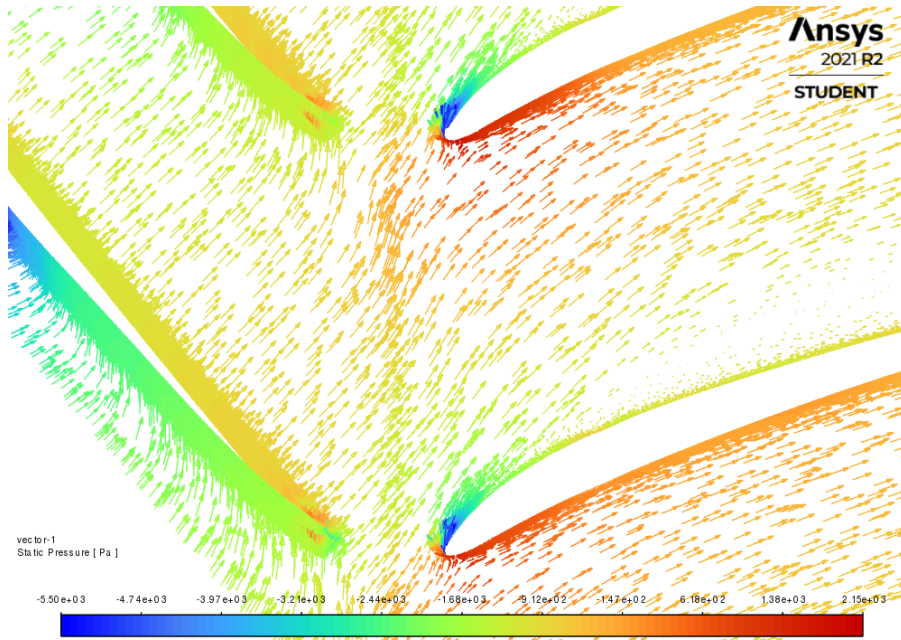


Figure 5.6: Velocity vector field colour per gauge static pressure at $t = 0.166\text{ s}$ (using a limited colour bar range)

The discussion until now explains why the static pressure can increase in the system. However, to do so, the velocity of the fluid needs to be increased ahead of the stator. This is investigated in Figure 5.7.

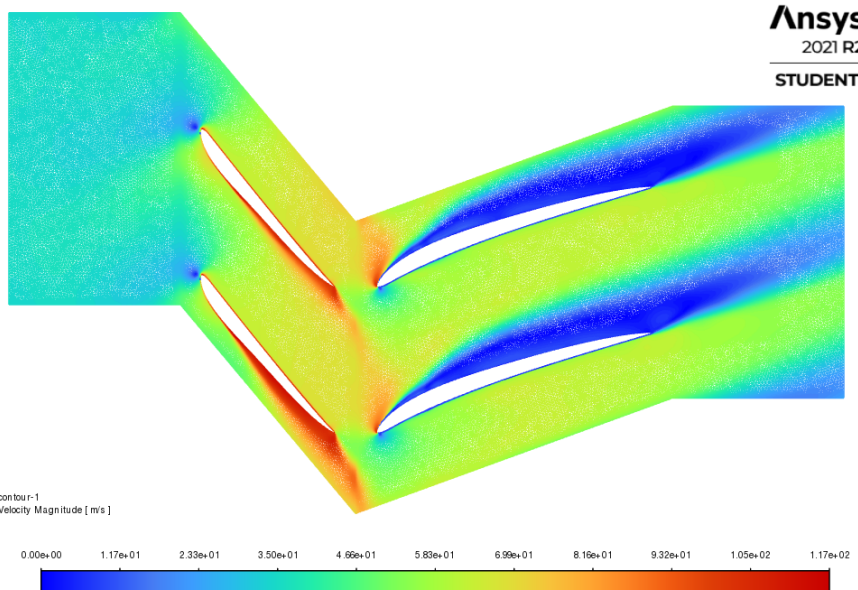
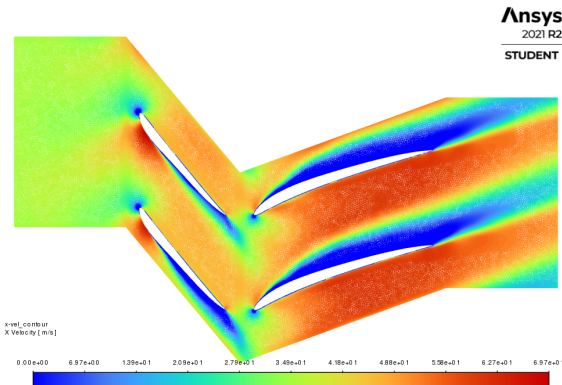
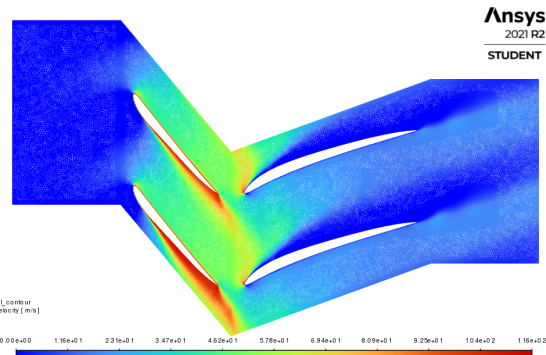


Figure 5.7: Velocity magnitude contours on the domain at $t = 0.166\text{ s}$

From Figure 5.7, it is clear that the rotor gives energy to the flow by accelerating it massively compared to the inlet velocity. It is furthermore clearly seen that the stator acts like an obstacle to the flow incoming from the rotor. It clearly creates a region, with little to no incoming flow, in the same way as a wall in a pipe would. By analysing the contours of the x- and y-velocity components shown in Figure 5.8, more insights on the flow behaviour can be obtained.



(a) Contour of the horizontal velocity component



(b) Contour of the vertical velocity component

Figure 5.8: Contours of the velocity components at $t = 0.166\text{ s}$

Clearly, from Figure 5.8a, the horizontal velocity is increased after going through the rotor. This is due to the tilt of the airfoil, which pushes the fluid both up and to the right. The gained x-velocity is the relatively conserved over the stator, however the y-velocity is directly lost as the flow encounters the stator (which is the process increasing the static pressure).

From the results derived above, it is clear that the geometry is able to compress the flow by accelerating it using the rotor and using the stator as an obstacle (meaning that as the fluid encounters the stator, its velocity drops while its static pressure increases). The streamlines of the fluid through the axial compressor are shown in Figure 5.9.

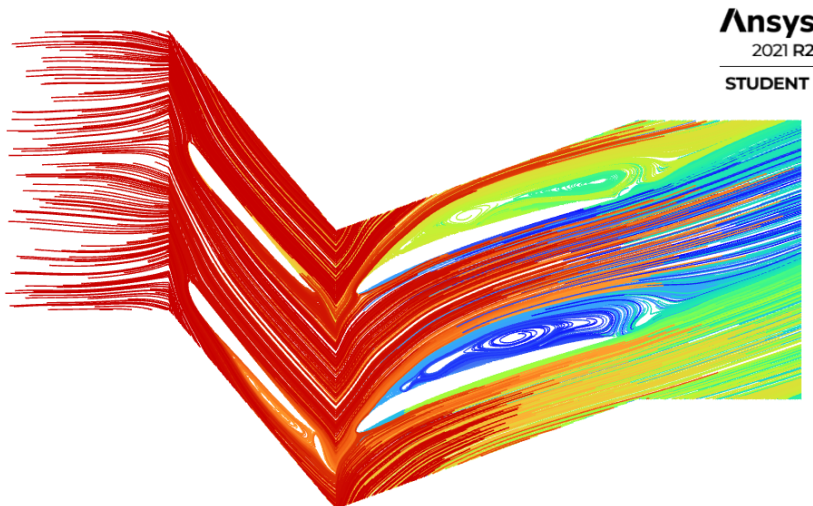


Figure 5.9: Streamlines of the fluid through the axial compressor at $t = 0.166\text{ s}$

As will be analysed in further depth in the next section, it is obvious from Figure 5.9 that a separation bubble occurs on the stator airfoils but not on the rotor airfoils. From this contour plot, it can furthermore be argued that the way the flow travels in the system is physical (meaning that no obvious error is present in the modelling). The streamlines also confirm the interpretation from the previous results, as the flow particles seem to encounter the stator as an obstacle after going through the rotor-stator interface.

The behaviour of both the temperature and density within the system can also be interesting for design purposes. The contour plots for temperature and density respectively can be seen in Figures 5.10 and 5.11.

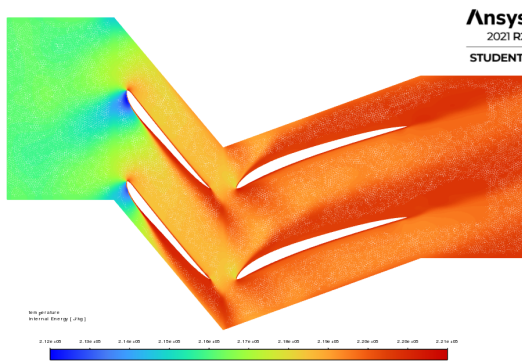


Figure 5.10: Static temperature contour at $t = 0.166\text{ s}$

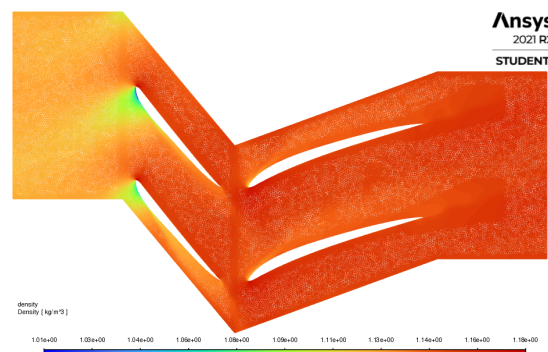


Figure 5.11: Density contour at $t = 0.166\text{ s}$

As expected, Figure 5.10 shows that the static temperature (and thus the internal energy) of the fluid is increased through the stage. More specifically, the dynamics of the rotor gives energy to the flow, which raises the fluid temperature. Considering Figure 5.11, the density of the fluid increases over the system, however, more details can be seen in Figure 5.12 by adapting the range to exclude the minimum which can be found at the leading edge of the rotor blade.

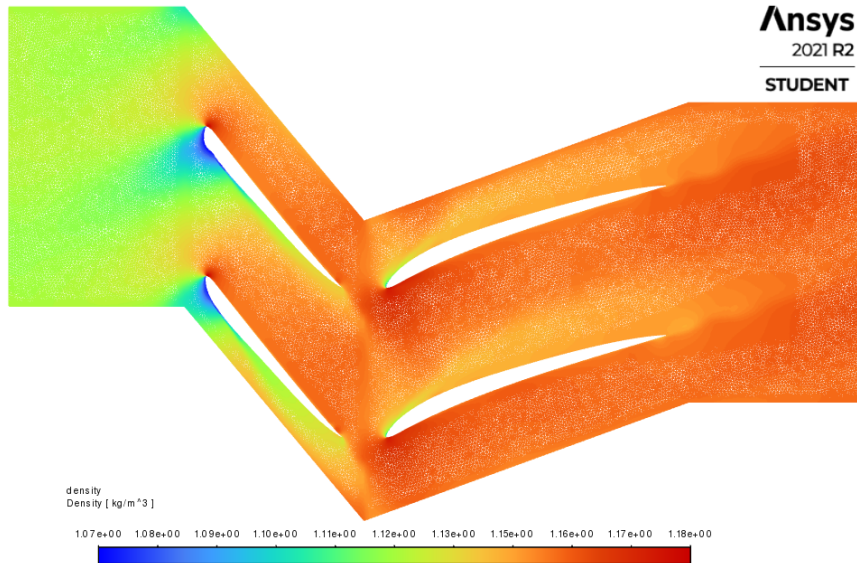


Figure 5.12: Density contour of the flow at $t = 0.166\text{ s}$ after excluding the minimum of the domain

Note that in Figure 5.12, the rotor blades are truncated at the leading edge, as the range of values was adapted to exclude the minimum. Furthermore, this contour plot shows a lot of insight to verify the interpretation on the process of compression that was presented earlier. In the rotor region, the air below the blade is sucked as the airfoil moves upwards (showing a lower density region) and the air above is accumulated (and hence rising the density). Then, the density increases at the leading edge and lower side of the stator blades as the airflow encounters the obstacle, while the density is lower on the upper side due to less incoming air in those regions.

Furthermore, the flow is expected to be turbulent behind the stator region. This is checked through contour plots of the Turbulent Intensity and Turbulent Kinetic Energy (k), shown in Figures 5.13 and 5.14.

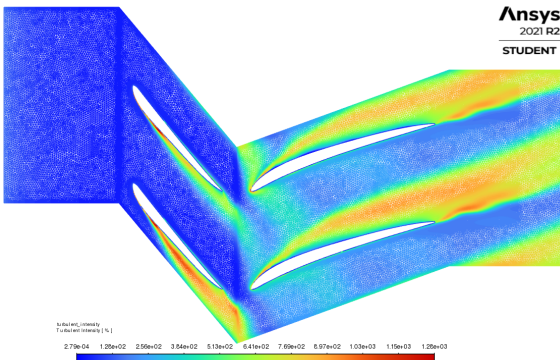


Figure 5.13: Turbulent intensity of the flow at $t = 0.166\text{ s}$

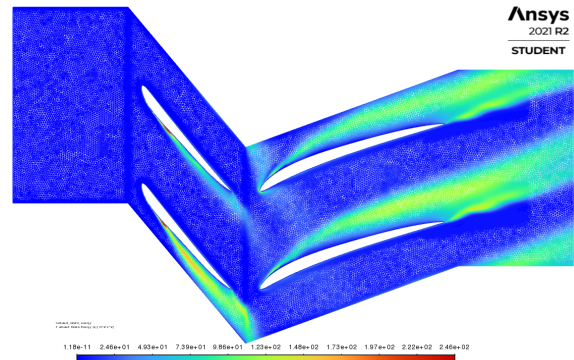


Figure 5.14: Turbulent kinetic energy of the flow at $t = 0.166\text{ s}$

From Figures 5.13 and 5.14, it can be seen that turbulence is very present behind the stator, as was expected (and was anticipated by refining the region behind the airfoil and on the airfoil itself). However, it is also found that the flow below the rotor is also quite turbulent and would require a better mesh refinement in this region for a further iteration of the project. Those regions with large TKE contain a lot of energy, probably inducing some recirculation of the flow, as will be seen later.

In order to analyse the flow, a snapshot at $t = 0.166 \text{ s}$ (equivalent to 100 cycles) was used. Although the flow is unsteady due to the movement of the rotor, the general flow characteristics are so-called "unsteady periodic" and analysing the snapshot gives a general overview of the flow at all times. This can be confirmed by looking at the contour plot of one such general characteristics at different subsequent instants of time, as is seen in Figure 5.15.

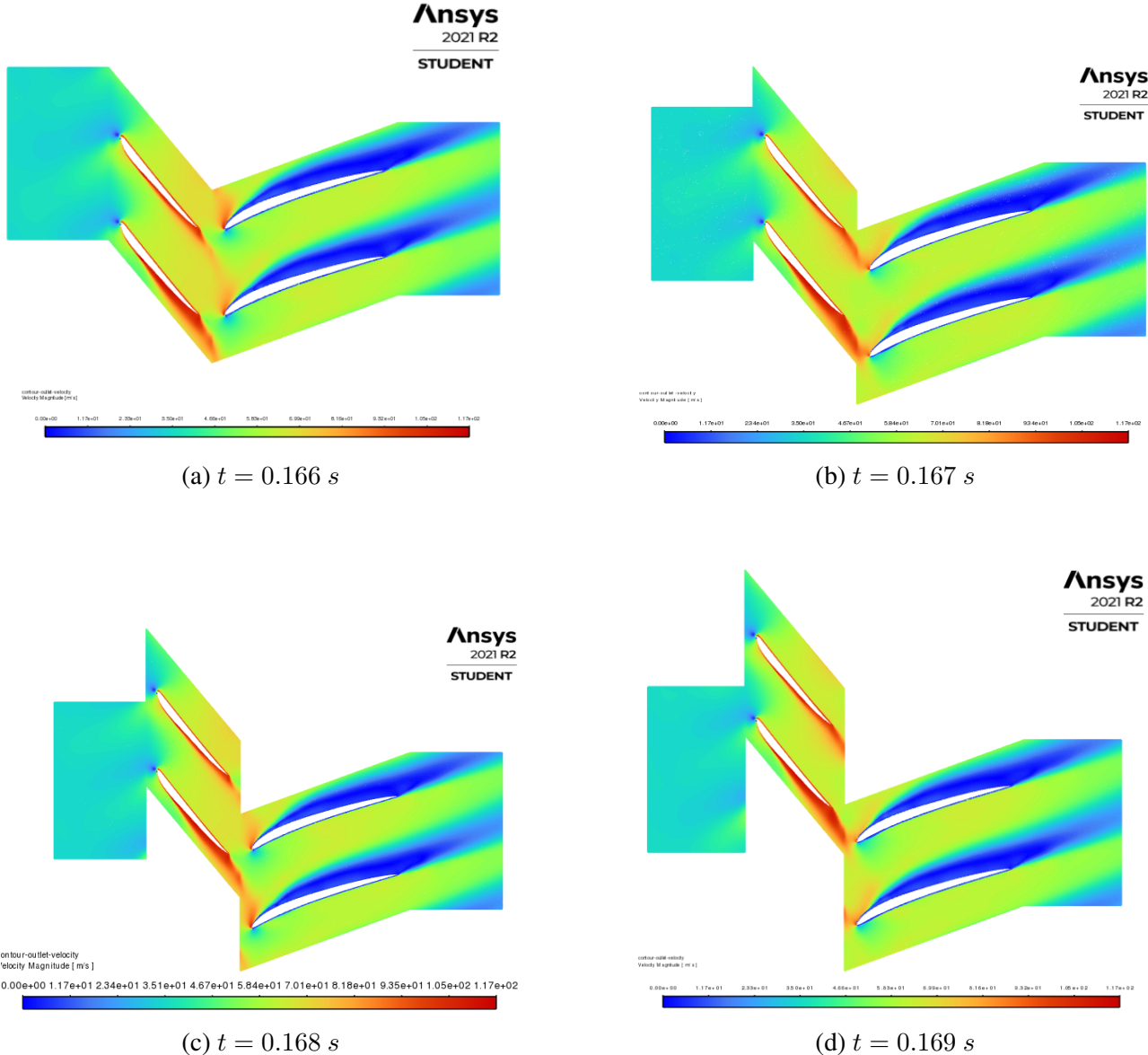


Figure 5.15: Velocity magnitude contour of different subsequent time instants

Looking at the different time steps from Figure 5.15, it can be seen that an unsteady periodic solution was reached for the overall flow properties. This can be argued as clearly only a translation upward of the rotor region is happening while the general flow behaviour does not change. Only the different flow phenomena occurring precisely at the interface are different due to the relative position of the rotor blades with respect to the stator blades. Therefore, analysing the general flow characteristics during one snapshot is deemed sufficient.

5.4 Flow Around the Airfoils

In this section, the flow analysed closer to the airfoils is analysed rather than general flow properties. The goal is to understand further the flow in the system by focusing on its main part: the blades. To do so, the streamlines around the rotor and stator are plotted in Figure 5.16.

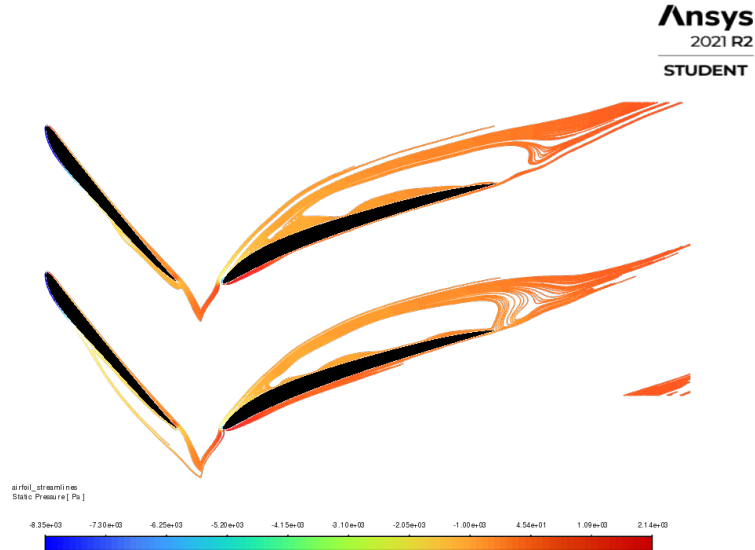


Figure 5.16: Streamlines around the airfoils coloured by static pressure at $t = 0.166\text{ s}$ (modified from ANSYS)

Note that a slight separation is occurring on the second rotor, but not the first one, although everything is supposed to be periodic (hence same flow on both rotors is expected). This could be the case due to a slight imperfection in the geometry or the flow not being fully converged actually. Furthermore, the sharp angle made by the flow at the interface shows that the fluid goes from the rotor reference frame to the stator reference frame, showing the expected relative velocity of the flow with respect to the stator. It can be seen from Figure 5.16 that full separation occurs on the stator. This is caused by the relative angle of attack of the airfoil with respect to the flow (which has gained a y -velocity component from the effect of the rotor movement). This zone of complete separation induces turbulence as could be seen on Figures 5.13 and 5.14, such turbulence is furthermore translated into recirculation of the flow in the separated boundary layer. This can be seen in Figure 5.17.

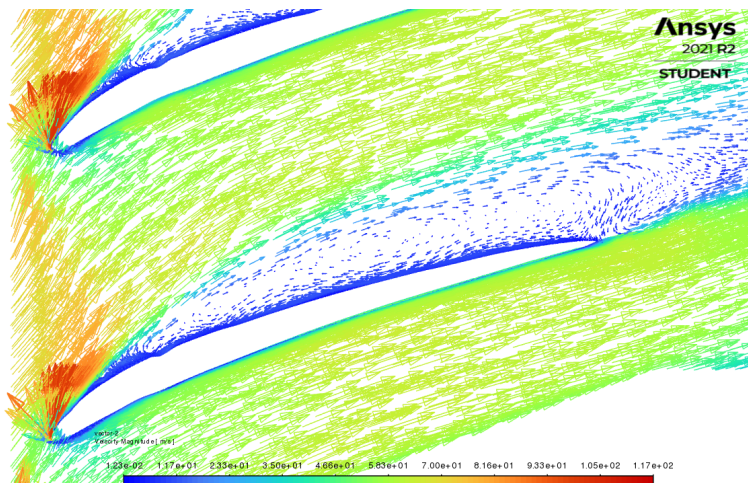


Figure 5.17: Recirculation of the flow behind the stator coloured by velocity magnitude at $t = 0.166\text{ s}$

A similar, yet lesser effect is seen below the rotor as partial separation occurs. The pressure coefficient graphs of both airfoil types can be examined to better understand the separation of the flow. Those can be seen on Figure 5.18. Note that the pressure coefficient at the stagnation point significantly larger than 1 shows that the flow is indeed (very) compressible. This further justifies the use of the compressible flow model.

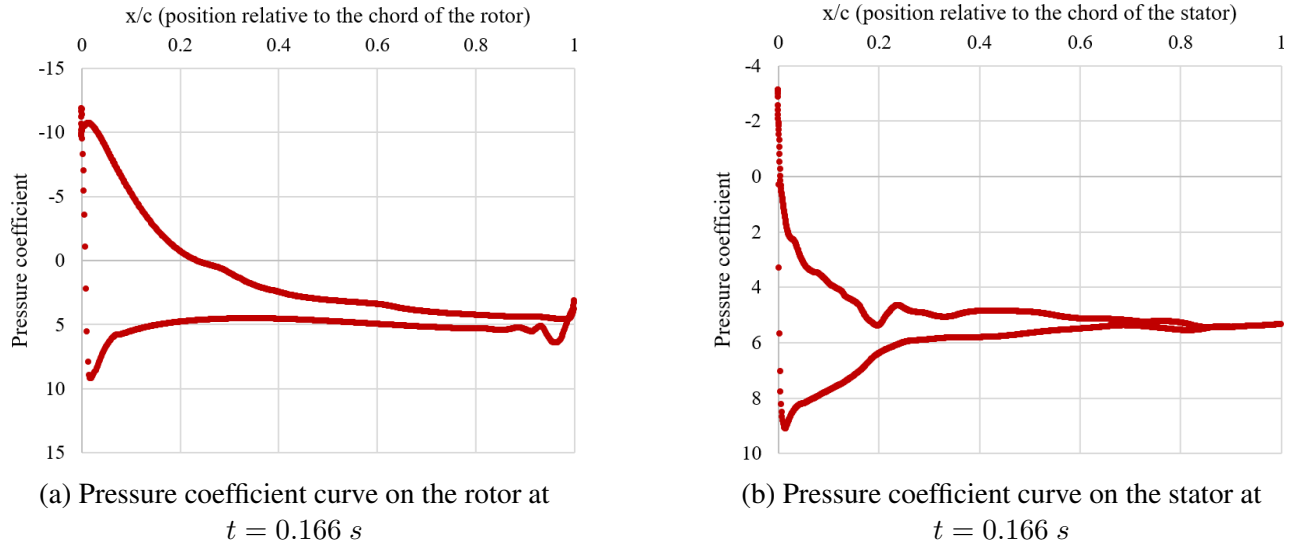


Figure 5.18: Pressure coefficient curves on the rotor and stator at $t = 0.166 \text{ s}$

In Figure 5.18 the upper side of the airfoils is the top curve and the lower side is the bottom curve. The plots were obtained using the inlet flow characteristics given in Table 5.1 as free stream in the definition of pressure coefficient: $C_p = \frac{p-p_\infty}{\frac{1}{2}\rho_\infty V_\infty}$.

Table 5.1: Inlet flow characteristics used as free stream quantities

Flow Property	Value
Area	1 m^2
Density	1.150527 kg/m^3
Pressure	$-4,500 \text{ Pa}$
Temperature	300 K
Velocity	35 m/s
Viscosity	$1.789410^{-5} \text{ kg/(ms)}$

Separation usually happens due to a high pressure gradient in the on the airfoil, characterised by a large slope in the pressure coefficient graphs. Looking at Figure 5.18, it is possible to confirm the results deduced in Figure 5.16 as the larger pressure gradients are seen on the upper surface of the stator at the leading edge (indicating a full separation) and on the lower side of the 2nd rotor shortly after the leading edge.

5.5 Comparison with Frozen Rotor-Stator Case

A comparison between the results obtained in the steady and unsteady simulations is fundamental to ensure the validity of the convergence study. Indeed, to verify that the mesh studied in steady conditions are valid in unsteady ones, it is necessary to prove that the velocity gradients are similar

and are found in the same regions of the geometry. In Fig. 5.19 the velocity contours of the steady situation are shown. It is evident that the large gradients are located in the same zones of the unsteady situation, displayed in Fig. 5.7. When the flow runs into the rotor and stator blades, there is an immediate variation in velocity in correspondence with the leading edges.

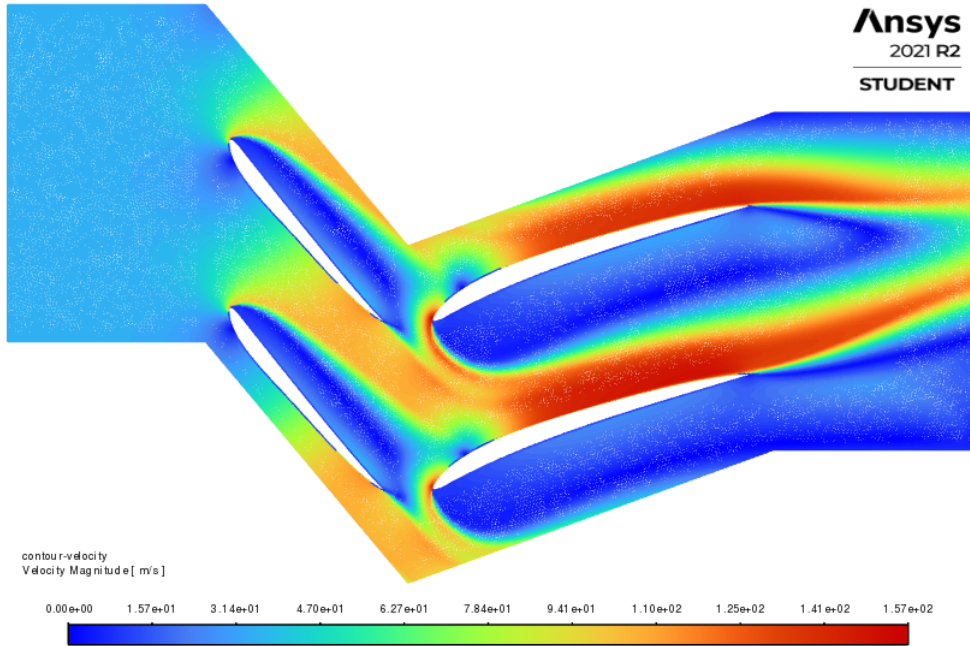


Figure 5.19: Velocity contours in steady state

A similar behaviour is observed in the unsteady case. In Fig. 5.20 and 5.21, a comparison between the two cases is shown. The orders of magnitude for velocity are the same in both case studies, and the main variations happen in proximity of the blades, where the mesh is finer.

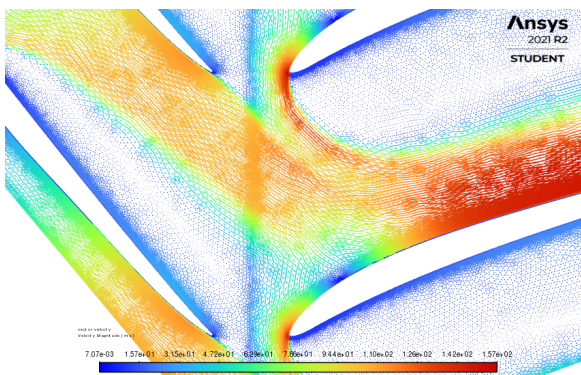


Figure 5.20: Velocity vector field in steady situation

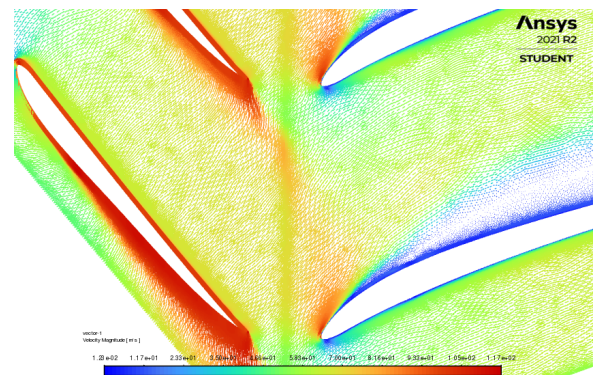


Figure 5.21: Velocity vector field in unsteady situation

Additionally, it is interesting to observe the general flow behaviour of the unsteady and steady case. As this is not the main focus of the study, only the most notable differences will be pointed out. First of all, the general velocity field can be looked at, which shows additional results to the velocity gradients previously analysed. It is possible to observe, that the regions of high and low velocity are located differently for the steady and unsteady case. In the unsteady case, as shown in Figure 5.7, a small layer of high velocity is observed at the bottom of the rotor blades, but in general the velocity in the rotor region is homogeneous. At the stator, it can be seen that the flow velocity above the stator is significantly lower than below the stator. This can be explained by the fact that the flow is pushed

up by the movement of the rotor, leading to a high relative angle of attack of the flow with respect to the blade, which can also be seen in Figure 5.9. As a result of this, separation occurs above the stator blades.

For the steady case in Figure 5.19, it can be observed that separation occurs both above the rotor blades and below the stator blades. Those differences can be explained by the steadiness of rotor. At the rotor blades, due to the missing movement of the rotor, the flow now sees a very high angle of attack, which causes separation at the upper side of the blade. When leaving the rotor region, instead of being pushed up, as it is the case in the unsteady simulation, the flow direction in the steady simulation is now directed downwards. As a consequence, the flow is directed nearly vertically on the upper surface of the stator blades, as can be seen more in detail in Figure 5.20. With respect to the flow, the stator blade is now seen as a reversed airfoil blade with an extremely high angle of attack. This explains the separation at the bottom surface, which is exactly the opposite compared to the unsteady case.

In addition to the velocity magnitude, the static pressure of both cases will be compared. The pressure contours plots of the steady and unsteady simulation are shown in Figure 5.22 and Figure 5.23. As can clearly been observed, the flow is compressed in the unsteady simulation, so the compressor fulfills its task. For the steady simulation, the flow is not compressed and even seems to be expanded. While the pressure field seems to be very homogeneous in the unsteady case, with only high pressure gradients observed at the leading edge of the rotor, the steady simulation shows multiple regions with high pressure gradients.

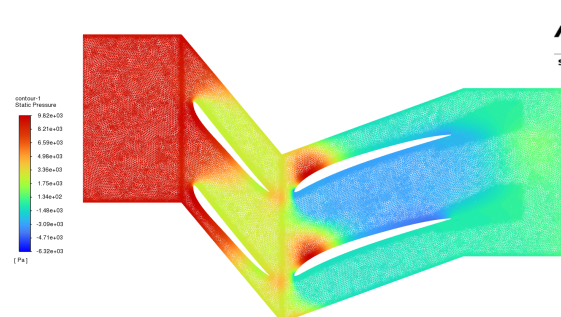


Figure 5.22: Pressure contour in steady situation

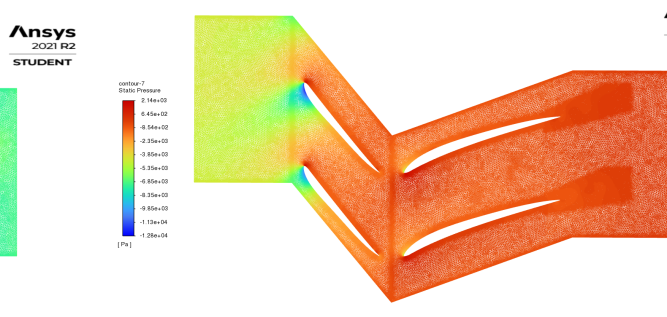


Figure 5.23: Pressure contour in unsteady situation

In the steady simulation, high pressure gradients can especially be observed above the rotors leading edge and at the front part of the stators upper surface. The former can be explained by the separation at the rotor, which has been observed in Figure 5.19. The high gradients above the stator can also be explained by a phenomena which has already been discussed for the velocity field: As the flow is directed vertically on the stator upper surface, which has been observed in Figure 5.20, it is stuck on the stators surface and the velocity suddenly decreases. Consequently an increase in static pressure is created and can be observed in Figure 5.22. The generally high gradients and the non-homogeneous pressure field in the steady simulation are due to the fact that a compressor is optimized for compressing the flow in an unsteady case and is not developed to be used in a steady application. The observed differences are therefore expected results for this comparison.

Conclusion 6

The purpose of this report was to analyse the flow properties such as velocity and pressure through a rotor-stator stage. Special attention was paid to the pressure difference over the compressor stage in order to verify if it fulfills its compressing task. The study was performed by creating a rotor-stator stage from scratch by correctly defining the problem using the properties of a subsonic compressor. A suitable mesh was chosen, in order to obtain the most accurate results possible while limiting the computational time for running the simulation. The choice of the numerical methods as well as of the mesh was important in order to be able to observe and model all relevant flow phenomena, such as turbulence. The results obtained in ANSYS Fluent were then analysed by especially focusing on pressure and velocity characteristics of the flow.

The geometry used for this study is a 2-dimensional simplification of a 3-D rotor-stator stage of a compressor, composed of two couples of typical rotor and stator blades of a subsonic axial compressor. An unsteady simulation problem was defined using a flow of compressible ideal gas with a $k - \omega$ turbulence model. A sliding mesh was used in order to model movement of the rotor and periodic boundary conditions allow to imitate an actual cylindrical compressor. An unstructured mesh was chosen with a refinement at particularly important regions of the flow, as for example the stator wake, and an inflation boundary layer was chosen, which is verified to correctly model the turbulent blow around the blades. A convergence study was performed in order to chose the best refinement factor for the mesh for obtaining accurate results for the flow characteristics.

Results were obtained on the optimal mesh after convergence at around 1660 simulation time steps. As was expected for the compressor stage, a pressure increase (approximately 4455 Pa) is observed in the simulation. This is due to an acceleration of the flow velocity at the rotor, which raises the energy of the flow. The following stator then slows down the flow again and thus causes an increase of static pressure of the flow. The average flow velocity increases from 35 to 39.2 m/s between the inlet and the outlet. As was expected and anticipated by modelling, the flow behind the stator shows a turbulent behaviour. When analyzing the results, more specific attention was paid to the separation above the airfoil blades, which follows from high pressure gradients on the airfoil. The discussed turbulence also favors turbulence of the flow, as was observed from the results. Finally, it was verified that the use of one snapshot in time was valid by looking at the flow in different instants of time in one cycle and observing the overall flow properties especially behind the stage remained the same.

A final additional comparison between the steady simulation used for the convergence study and the unsteady simulation used to obtain the results was performed. It was observed, that the regions of high gradients of the flow mostly coincide, but that the overall flow looks different for both cases. This is however an expected outcome of the comparison, as only the movement of the rotor creates the anticipated pressure difference over the compressor stage. In conclusion, it was confirmed that the simulation provides meaningful and valuable results and that the rotor-stator stage correctly performs its task of compressing the flow, even if the design is a simplification and could further be optimized for optimal compression of the flow.

The following recommendations are suggested by the authors in order to improve the obtained results:

- The geometry used in this report considers two airfoils per row, effectively doubling the number of mesh cells. This was done in order to offer better visualization of the flow phenomena

between the airfoils, however, if more focus is given to the numerical values of the properties, only one airfoil in each row would be necessary. This would reduce the computational load and permit greater accuracy of the results.

- As suggested by the convergence study, the work presented in this report was limited by the options of the ANSYS student licence, limiting the total number of mesh cells to 500,000. Using a licence allowing for a finer mesh could be desirable in order to further refine the results and ensure a proper convergence of the method.
- In order to minimize the computational time, the solvers used were all first order in this work. To improve the accuracy of the results, second order solvers can be used in a next iteration of the project.
- A mass imbalance issue was found in the simulation results. The authors recommend investigating the issue in more details as it could invalidate parts of the results observed. Possibilities to solve the problem include extending the outlet and inlet sections, and letting the simulation run for longer than 1660 time steps as done in the current work. Neither of those suggestions was tried in the frame of this work due to time constraints.
- Following the analysis of the turbulence intensity and kinetic energy, it was found that more complex flow phenomena than first expected can be found on the lower side of the rotor airfoils. The authors recommend a further refinement of the mesh in this region to allow for more accurate computational results.

References

- [1] P. I. J. van Buijtenen and I. W. Visser, *Gas turbines*, 1st, Delft University of Technology, Feb. 2011.
- [2] M. Schnoes and E. Nicke, *Exploring a Database of Optimal Airfoils for Axial Compressor Design*. German Aerospace Center (DLR) Institute of Propulsion Technology: Publisher, 2017.
- [3] C. Barberi *et al.*, “Validation of steady and unsteady cfd strategies in the design of axial compressors for gas turbine engines,” *Aerospace Science and Technology*, vol. 107, no. 106307, 2020.
- [4] M. A. Khan, P. Arunagiri, and G. A. S. Prabu, “Parametric investigation on a transonic axial compressor stage using cfd techniques,” *Materials Today: Proceedings*, vol. 33, no. 912-18, 2020.
- [5] L. Kumar and D. B. Alone, “Design and cfd analysis of a multi stage axial flow compressor,” *Propulsion Division CSIR-National Aerospace Laboratories, Bangalore, India -560017*, 2019.
- [6] L. E. Ferrer-Vidal, A. Iglesias-Pérez, and V. Pachidis, “Characterization of axial compressor performance at locked rotor and torque-free windmill conditions,” *Aerospace Science and Technology*, vol. 101, no. 105846, 2020.
- [7] A. Barettter *et al.*, “Experimental and numerical analysis of a compressor stage under flow distortion,” *International Journal of Turbomachinery, Propulsion and Power*, vol. 6, no. 43, 2021.
- [8] M. T. Shobhavathy and P. Hanoca, “Cfd analysis to understand the flow behaviour of a single stage transonic axial flow compressor,” *ASME 2013 GAS TURBINE INDIA CONFERENCE*, 2013.
- [9] R.-J. Yang and S.-J. Lin, “Numerical solutions of 2-d multi-stage rotor/stator unsteady flow interactions,” in *NASA, Lewis Research Center, Computational Fluid Dynamics Symposium on Aeropropulsion*, 1991.
- [10] E. Outa, D. Kato, and K. Chiba, “An ns simulation of stall cell behavior in a 2-d compressor rotor-stator system at various loads,” in *Turbo Expo: Power for Land, Sea, and Air*, American Society of Mechanical Engineers, vol. 78835, 1994, V001T01A093.
- [11] Q. Xiaoqing, W. Songtao, F. Guotai, and W. Zhongqi, “Aerodynamic design and analysis of a low-reaction axial compressor stage,” *Chinese Journal of Aeronautics*, vol. 21, no. 1, pp. 1–7, 2008.
- [12] Y. P. Rangel, *Axial compressor*, Apr. 2020. [Online]. Available: %5Curl%7Bhttps://grabcad.com/library/axial-compressor-6%7D.
- [13] ANSYS *Fluent User’s Guide*, 2021 R2 ed. ANSYS, Inc., 2021.
- [14] ANSYS *Fluent Theory Guide*, 2021 R2 ed. ANSYS, Inc., 2021.
- [15] E. Shashi Menon, “Chapter three - physical properties,” in *Transmission Pipeline Calculations and Simulations Manual*, E. Shashi Menon, Ed., Boston: Gulf Professional Publishing, 2015, pp. 29–82, ISBN: 978-1-85617-830-3. DOI: <https://doi.org/10.1016/B978-1-85617-830-3.00003-1>. [Online]. Available: <https://www.sciencedirect.com/science/article/pii/B9781856178303000031>.

- [16] E. Boujo, *Course slides Numerical Flow Simulation*, Available on the Moodle course page of Numerical Flow Simulation, 2021.
- [17] Joe Honeywell. “Important aspects of centrifugal compressor testing – part 2.” (2010), [Online]. Available: <http://www.jmcampbell.com/tip-of-the-month/2010/09/important-aspects-of-centrifugal-compressor-testing-part-2/>.